Computational Geosciences (2022) 26:53–70
https://doi.org/10.1007/s10596-021-10108-4

ORIGINAL PAPER

A stable space-time FE method for the shallow water equations

Eirik Valseth[1] · **Clint Dawson**[1]

Received: 30 April 2021 / Accepted: 28 September 2021 / Published online: 15 November 2021

Abstract

We consider the finite element (FE) approximation of the two dimensional shallow water equations (SWE) by considering discretizations in which both space and time are established using a stable FE method. Particularly, we consider the automatic variationally stable FE (AVS-FE) method, a type of discontinuous Petrov-Galerkin (DPG) method. The philosophy of the DPG method allows us to establish stable FE approximations as well as accurate *a posteriori* error estimators upon solution of a saddle point system of equations. The resulting error indicators allow us to employ mesh adaptive strategies and perform space-time mesh refinements, i.e., local time stepping. We establish *a priori* error estimates for the AVS-FE method and linearized SWE and perform numerical verifications to confirm corresponding asymptotic convergence behavior. In an effort to keep the computational cost low, we consider an alternative space-time approach in which the space-time domain is partitioned into finite sized space-time slices. Hence, we can perform adaptive mesh refinements on each individual slice to preset error tolerances as needed for a particular application. Numerical verifications comparing the two alternatives indicate the space-time slices are superior for simulations over long times, whereas the solutions are indistinguishable for short times. Multiple numerical verifications show the adaptive mesh refinement capabilities of the AVS-FE method, as well the application of the method to some commonly applied benchmarks for the SWE.

Keywords Shallow water equations · Discontinuous Petrov-Galerkin · Adaptivity · Space-time FE method · Local time stepping

Mathematics Subject Classification (2010) 65M60 · 35A35 · 35L65 · 35Q35

1 Introduction

The shallow water equations govern the flow of water in domains in which the characteristic wavelength horizontally is significantly larger than the depth of water. A very important application of the SWE is in the modeling of events such as storm surges resulting from hurricanes. Thus, the importance of accurate numerical solution techniques should therefore be clear as the repercussions of such events can be vast. The SWE are surrogates for the Navier-Stokes equations in which the direction of the depth has been integrated from the sea floor to the free surface of the water and application of the corresponding boundary conditions. The resulting equations are continuity and momentum equations for the water surface elevation and depth-averaged horizontal velocities, respectively. Generally, the domains of interest in the application of the SWE are irregular and the resulting computational meshes need to be unstructured, thereby making FE methods well suited for the numerical approximation of the SWE, see, e.g., [31, 41] for early examples.

For flow regimes resulting from hurricanes, the motion of the water, i.e., convection is the driving mechanism of transport. The domination of convective transport over diffusive transport leads to discrete stability issues in the Galerkin FE method. This issue is well known to be resolved when the element size in the FE mesh is adequately refined near phenomena such as interior or boundary layers. However, the computational cost and the required mesh generation efforts on a case-by-case basis is generally prohibitive. Furthermore, the smallest element size dictates the corresponding time step size further increasing the computational cost. Lynch and Gray developed the wave continuity equation as

This work has been supported by the United States National Science Foundation - NSF PREEVENTS Track 2 Program, under NSF Grant Number 1855047.

✉ Eirik Valseth
eirik@utexas.edu

[1] Oden Institute for Computational Engineering and Sciences, The University of Texas at Austin, Austin, TX 78712, USA

a surrogate for the SWE in [36] which results FE approximations with better stability properties than the SWE. The wave continuity equation is employed in the advanced circulation model of Luettich et al. [35], which is widely used and has been developed to encompass a wide range of features important in hurricane storm surge modeling.

Discontinuous Galerkin (DG) methods as well as their hybridized versions [27, 48, 53] are popular FE methods for the SWE. Important reasons for their popularity include high accuracy, their mass conservation property, ease of establishing conditionally stable FE discretizations, and local p-adaptivity [32]. Recently, high order entropy stable DG methods for curved FE meshes have been introduced for the SWE by Wu et al. in [54] which satisfies discrete conservation of entropy. The entropy stable method takes ad vantage of summation-by-parts operators to increase computational efficiency compared to traditional DG methods and is demonstrated through numerical verifications. The development of hybridized DG (HDG) methods has also reduced the computational cost of solving the global system of equations compared to standard DG methods [48]. Coupled Galerkin and DG methods have also successfully been developed to maximize efficiency and accuracy by Dawson and Proft in [15, 16]. Least squares FE methods (LSFEMs) [7] have also been successfully applied to the SWE by Starke in [49] and Liang and Hsu in [34]. Both these LSFEMs take advantage of the stability property of LSFEMs spatially and the authors present several numerical verifications.

The aforementioned FE methods used in shallow water systems for the SWE or its surrogate wave continuity equation employ a method of lines approach in the temporal discretization. Thus, spatial and temporal computations are decoupled, where finite elements are employed in space and time stepping schemes such as finite difference methods are employed in time. It is less common to employ space-time FE methods, i.e., using FE discretizations of both space and time. The main reasons are likely the increased computational cost of such methods, as well as the inherently unstable numerical nature of Galerkin FE methods for first order partial derivatives. However, some examples of space-time FE methods for the SWE do exist in literature [3, 43, 44, 51], where discrete stability is ensured in space and time by an upwinding argument. In modern multi processor computers and supercomputers, the additional cost of space-time FE methods can be justified as the functional framework of FE leads to readily available *a priori* error bounds in addition to *a posteriori* error estimation techniques. Hence, space-time FE methods can take advantage of adaptive mesh refinement strategies to maximize computational efficiency and accuracy.

The AVS-FE method [10] is a stable FE method that falls into the category of minimum residual methods, e.g., the discontinuous Petrov-Galerkin (DPG) method, [12, 17–20] and least squares FE methods [7]. The stability of the DPG method is ensured by a particular choice of test functions which is defined by a Riesz representation problem that realize the supremum in the *inf-sup* condition. The corresponding FE approximations of a partial differential equation (PDE) is achieved by computing on-the-fly optimal test functions and solving a symmetric positive definite system of equations. This method remains attractive in particular due to its discrete stability property, regardless of the differential operator. Additionally, according to the philosophy of the DPG method, the AVS-FE method establishes an equivalent saddle point system which yields both the AVS-FE approximate solution of the PDE, as well as an "error representation function". This function leads to *a posteriori* error estimates of the numerical approximation error in terms of an energy norm.

Following this introduction, we introduce the model initial boundary value problem (IBVP) as well as notations and conventions in Section 2.1. In Section 2.2, we present the equivalent AVS-FE weak formulation and its analysis for the SWE IBVP. *A priori* error estimates are introduced in Section 3. In Section 4, we perform multiple numerical verifications for the SWE presenting numerical asymptotic convergence properties as well $h-$adaptive refinements of the space-time FE mesh. Finally, we conclude with remarks on the results and future works in Section 5.

2 The shallow water equations and the AVS-FE method

2.1 Model problem: the shallow water equations

The derivation of the SWE from the three-dimensional incompressible Navier–Stokes equations is performed under the assumptions of a long horizontal wavelength and hydrostatic pressure distribution, see, e.g. [26]. Let $\Omega \subset \mathbb{R}^2$ be a bounded open domain with a Lipschitz boundary $\partial\Omega$ which is partitioned into two segments Γ_{I} and Γ_{O}, such that $\partial\Omega = \overline{\Gamma_{\mathrm{I}} \cup \Gamma_{\mathrm{O}}}$. For simplicity we also consider the domain Ω to be convex. Also, let $\mathbf{n}$ be the outwards unit normal vector to the global boundary, and identify the boundary segments as $\Gamma_{\mathrm{I}} = \{\mathbf{x} \in \partial\Omega \ : \ \mathbf{u}\cdot\mathbf{n} < 0\}$ and $\Gamma_{\mathrm{O}} = \{\mathbf{x} \in \partial\Omega \ : \ \mathbf{u}\cdot\mathbf{n} \geq 0\}$ as in and outflow boundaries, respectively. Finally, define the temporal domain $t \in (0, T) \subset \mathbb{R}_0^+$. Hence, we consider the following version of the viscous two dimensional SWE [15, 16]:

$$\frac{\partial \zeta}{\partial t} + \nabla \cdot (\mathrm{H}\mathbf{u}) = 0, \tag{1a}$$

$$\frac{\partial \mathbf{u}}{\partial t} + \mathbf{u}\cdot(\nabla\mathbf{u}) + \tau_{bf}\,\mathbf{u} + g\nabla\zeta - \mu\Delta\mathbf{u} = \mathbf{f}, \tag{1b}$$

where $H = \zeta + h_b$, $h_b = h_b(\mathbf{x})$ is the bathymetry of the bottom surface (see Fig. 1), the unknowns $\zeta = \zeta(\mathbf{x}, t)$ and $\mathbf{u} = \mathbf{u}(\mathbf{x}, t) = \{u_x(\mathbf{x}, t), u_y(\mathbf{x}, t)\}^{\mathrm{T}}$ represent depth averaged elevation and velocity, respectively, $g = 9.81 m/s^2$ the constant of gravitational acceleration, μ the depth averaged turbulent viscosity, τ_{bf} the bottom friction factor, and $\mathbf{f}$ represent body forces.

The system (1) consists of two PDEs, the continuity (1a) for the depth averaged water column elevation and the momentum (1b) governing the depth averaged velocity. The bottom friction factor τ_{bf} is a source of another potential nonlinearity as multiple friction models depend on both velocity and water depth in a nonlinear fashion.

To establish an IBVP of the SWE which admits a unique solution, a proper combination of boundary conditions (BCs) and initial conditions (ICs) is needed. Since the SWE are derived from the Navier-Stokes equations, these conditions are not trivial to establish due to the chaotic nature of these PDEs. In this paper, we seek to establish stable FE approximations of the SWE, therefore, we only consider cases in which the resulting IBVP has a unique solution [42]. To this end, we consider the following boundary and initial conditions:

$$\begin{aligned} &\zeta = \hat{\zeta} \text{ on } \Gamma_{\mathrm{I}}, \\ &\mathbf{u} = \hat{\mathbf{u}} \text{ on } \partial\Omega, \\ &\zeta = \zeta_0 \text{ on } \Omega, \\ &\mathbf{u} = \mathbf{u}_0 \text{ on } \Omega. \end{aligned} \tag{2}$$

Combining the PDE (1) and the conditions (2) gives the SWE IBVP:

Find $(\zeta, \mathbf{u})$ such that:

$$\begin{aligned} &\frac{\partial \zeta}{\partial t} + \nabla \cdot (\mathrm{H}\mathbf{u}) = 0, \text{ in } \Omega \times (0, T), \\ &\frac{\partial \mathbf{u}}{\partial t} + \mathbf{u} \cdot (\nabla \mathbf{u}) + \tau_{bf}\, \mathbf{u} + g \nabla \zeta - \mu \Delta \mathbf{u} = \mathbf{f}, \text{ in } \Omega \times (0, T), \\ &\zeta = \hat{\zeta} \text{ on } \Gamma_{\mathrm{I}}, \\ &\mathbf{u} = \hat{\mathbf{u}} \text{ on } \partial\Omega, \\ &\zeta = \zeta_0 \text{ on } \Omega, \\ &\mathbf{u} = \mathbf{u}_0 \text{ on } \Omega. \end{aligned} \tag{3}$$

In the following, we shall use the following notations:

- inner products between vector valued functions are denoted with the single dot symbol "$\cdot$", and inner products between tensor valued functions are denoted by the colon or double dot symbol ": ".
- the operator ∇ is the spatial gradient operator.
- the operation $\nabla \cdot \boldsymbol{\sigma}$, $\boldsymbol{\sigma}$ being a matrix/tensor valued function, corresponds to a row-wise application of the divergence operator.
- h_m is the diameter of element K_m.
- $\mathbf{n}_m$ is the outwards unit normal vector to element K_m.

2.2 Weak formulation and AVS-FE discretization

The AVS-FE weak formulations are established by techniques used in mixed FE methods as well as the broken weak forms associated to DPG, DG, and first-order system least squares (FOSLS) methods. The first step is the partition of the computational domain into finite elements, i.e., into a FE mesh. Here, we take a space-time approach in which the entire space-time domain is to be discretized using finite elements. First, define the space-time domain Ω_{T}:

$$\Omega_{\mathrm{T}} \overset{\text{def}}{=} \Omega \times (0, \mathrm{T}),$$

and the partition $\mathcal{P}_h^T$ of Ω_{T} into elements K_m, is such that:

$$\Omega_{\mathrm{T}} = \mathrm{int}\Big(\bigcup_{K_m \in \mathcal{P}_h^T} \overline{K_m} \Big), \quad K_m \cap K_n = 0, \quad m \neq n. \tag{4}$$

Our goal is to employ continuous FE approximating functions as bases for the trial space, e.g., Lagrange or Raviart-Thomas functions. Hence, it is required to recast the IBVP (3) into a first order system by introducing a tensor-valued variable $\boldsymbol{\sigma}$:

$$\boldsymbol{\sigma} = \nabla \mathbf{u} \overset{\text{def}}{=} \begin{bmatrix} \frac{\partial u_x}{\partial x} & \frac{\partial u_x}{\partial y} \\ \frac{\partial u_y}{\partial x} & \frac{\partial u_y}{\partial y} \end{bmatrix}. \tag{5}$$

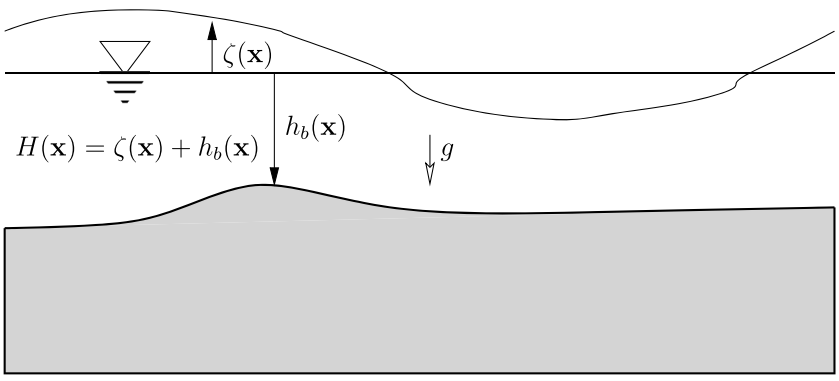

Fig. 1 Elevation and bathymetry overview

Using this variable, we recast the SWE IBVP into a first-order system:

Find $(\zeta, \mathbf{u}, \boldsymbol{\sigma})$ such that:

$$\begin{aligned}
&\frac{\partial \zeta}{\partial t} + \nabla \cdot (\mathbf{H}\mathbf{u}) = 0, \text{ in } \Omega_{\mathrm{T}},\\
&\frac{\partial \mathbf{u}}{\partial t} + \mathbf{u} \cdot (\nabla \mathbf{u}) + \tau_{bf}\, \mathbf{u} + g \nabla \zeta - \mu \nabla \cdot \boldsymbol{\sigma} = \mathbf{f}, \text{ in } \Omega_{\mathrm{T}},\\
&\boldsymbol{\sigma} - \nabla \mathbf{u} = \mathbf{0}, \text{ in } \Omega_{\mathrm{T}},\\
&\zeta = \hat{\zeta} \text{ on } \Gamma_{\mathrm{I}},\\
&\mathbf{u} = \hat{\mathbf{u}} \text{ on } \partial\Omega,\\
&\zeta = \zeta_0 \text{ on } \Omega_0,\\
&\mathbf{u} = \mathbf{u}_0 \text{ on } \Omega_0.
\end{aligned} \tag{6}$$

Hence, in the weak enforcement of (6), the required regularities of the trial variables are $\zeta \in H^1(\Omega_{\mathrm{T}})$, $\mathbf{u} \in H^1(\Omega_{\mathrm{T}})^2$, and $\boldsymbol{\sigma} \in H(\mathbf{div}, \Omega) \times L^2(0, T)$, where $H^1(\Omega_{\mathrm{T}})$ and $H(\mathbf{div}, \Omega)$ are the H^1 and $H(div)$ Hilbert spaces on Ω_{T} and Ω, respectively. In the following, we write $H(\mathbf{div}, \Omega)$ for $H(\mathbf{div}, \Omega) \times L^2(0, T)$.

The AVS-FE weak formulation is established by an element-wise weak enforcement of (6). The BCs and ICs are enforced in the strong sense and are incorporated into the trial space. Thus, the AVS-FE weak formulation is:

Find $(\zeta, \mathbf{u}, \boldsymbol{\sigma}) \in U(\Omega_{\mathrm{T}})$ such that:

$$B((\zeta, \mathbf{u}, \boldsymbol{\sigma}); (v, \mathbf{w}, \mathbf{p})) = F(v, \mathbf{w}, \mathbf{p}), \quad \forall (v, \mathbf{w}, \mathbf{p}) \in V(\mathcal{P}_h^T), \tag{7}$$

where $B : U(\Omega_{\mathrm{T}}) \times V(\mathcal{P}_h^T) \longrightarrow \mathbb{R}$, and the linear functional, $F : V(\mathcal{P}_h^T) \longrightarrow \mathbb{R}$ are defined:

$$\begin{aligned}
&B((\zeta, \mathbf{u}, \boldsymbol{\sigma}); (v, \mathbf{w}, \mathbf{p}))\\
&= \int_{\Omega_T} \Big\{ \frac{\partial \zeta}{\partial t} v + \nabla \cdot (\mathbf{H}\mathbf{u}) v \; + [\frac{\partial \mathbf{u}}{\partial t} + \mathbf{u} \cdot (\nabla \mathbf{u})\\
&\quad + \tau_{bf}\, \mathbf{u} + g \nabla \zeta - \mu \nabla \boldsymbol{\sigma}] \cdot \mathbf{w} + (\boldsymbol{\sigma} - \nabla \mathbf{u}) : \mathbf{p} \Big\}\, \mathbf{dx},\\
&F(v, \mathbf{w}, \mathbf{p}) = \int_{\Omega_T} \mathbf{f} \cdot \mathbf{w}\, \mathbf{dx},
\end{aligned} \tag{8}$$

and the function spaces $U(\Omega_{\mathrm{T}})$ and $V(\mathcal{P}_h^T)$ are defined:

$$\begin{aligned}
U(\Omega_{\mathrm{T}}) &\stackrel{\text{def}}{=} \Big\{ (\zeta, \mathbf{u}, \boldsymbol{\sigma}) \in H^1(\Omega_{\mathrm{T}})^3 \times H(\mathbf{div}, \Omega) :\\
&\mathbf{u}_{|\Omega_0} = \mathbf{u}_0, \zeta_{|\Omega_0} = \zeta_0, \zeta\,|_{\Gamma_{\mathrm{I}}} = \hat{\zeta}, \mathbf{u}|_{\partial\Omega} = \hat{\mathbf{u}} \Big\},\\
V(\mathcal{P}_h^T) &\stackrel{\text{def}}{=} L^2(\Omega_{\mathrm{T}})^7.
\end{aligned} \tag{9}$$

Note that the weak form (7) is a FOSLS weak form. We also define the following norm on the trial space, $\|\cdot\|_{U(\Omega_{\mathrm{T}})} : U(\Omega_{\mathrm{T}}) \longrightarrow [0, \infty)$

$$\begin{aligned}
\|(\zeta, \mathbf{u}, \boldsymbol{\sigma})\|^2_{U(\Omega_{\mathrm{T}})} \stackrel{\text{def}}{=} \int_{\Omega} \Big[&\nabla \zeta \cdot \nabla \zeta + \zeta^2 + \nabla \mathbf{u} : \nabla \mathbf{u}\\
&+ \mathbf{u} \cdot \mathbf{u} + (\nabla \cdot \boldsymbol{\sigma})^2 + \boldsymbol{\sigma} : \boldsymbol{\sigma} \Big]\, \mathbf{dx},
\end{aligned} \tag{10}$$

and the norm on $V(\mathcal{P}_h^T)$ is the standard L^2 norm:

$$\|(v, \mathbf{w}, \mathbf{p})\|^2 \stackrel{\text{def}}{=} \sum_{K_m \in \mathcal{P}_h^T} \int_{K_m} \Big[v_m^2 + \mathbf{w}_m \cdot \mathbf{w}_m + \mathbf{p}_m : \mathbf{p}_m \Big]\, \mathbf{dx}. \tag{11}$$

By inspection of the integral forms $B(\cdot;\cdot)$ and $F(\cdot)$ (8) and the function spaces $U(\Omega_{\mathrm{T}})$ and $V(\mathcal{P}_h^T)$ (9) it is easy to see that both forms are continuous by application of the Cauchy-Schwarz inequality. Next, we employ a FOSLS argument to show that $B(\cdot;\cdot)$ also satisfies the *inf-sup* condition. These arguments and further details can be found in [7, 49] for different least squares functionals and we present the arguments here for completeness, note that we assume a proper linearization of the nonlinear terms in $B(\cdot;\cdot)$ has been performed by $\mathcal{U}$ and $\mathcal{H}$ to establish the bilinear form $B_{\mathrm{lin}}(\cdot,\cdot)$:

$$\begin{aligned}
&B_{\mathrm{lin}}((\zeta, \mathbf{u}, \boldsymbol{\sigma}), (v, \mathbf{w}, \mathbf{p}))\\
&= \int_{\Omega_T} \Big\{ \frac{\partial \zeta}{\partial t} v + \mathcal{H} \nabla \cdot \mathbf{u} v \; + [\frac{\partial \mathbf{u}}{\partial t} + \mathcal{U} \cdot (\nabla \mathbf{u})\\
&\quad + \tau_{bf}\, \mathbf{u} + g \nabla \zeta - \mu \nabla \boldsymbol{\sigma}] \cdot \mathbf{w} + (\boldsymbol{\sigma} - \nabla \mathbf{u}) : \mathbf{p} \Big\}\, \mathbf{dx}.
\end{aligned} \tag{12}$$

We them pick the test functions to be $\mathbf{p} = \boldsymbol{\sigma} - \nabla \mathbf{u}$, $\mathbf{w} = \frac{\partial \mathbf{u}}{\partial t} + \mathcal{U} \cdot (\nabla \mathbf{u}) + \tau_{bf}\, \mathbf{u} + g \nabla \zeta - \mu \nabla \cdot \boldsymbol{\sigma}$, and $v = \frac{\partial \zeta}{\partial t} + \mathcal{H} \nabla \cdot \mathbf{u}$:

$$\sup_{(v, \mathbf{w}, \mathbf{p}) \in V(\mathcal{P}_h^T) \setminus \{0\}} \frac{|B_{\mathrm{lin}}((\zeta, \mathbf{u}, \boldsymbol{\sigma}), (v, \mathbf{w}, \mathbf{p}))|}{\|(v, \mathbf{w}, \mathbf{p})\|} \geq \frac{\left\| \left(\frac{\partial \zeta}{\partial t} + \mathcal{H} \nabla \cdot \mathbf{u}, \frac{\partial \mathbf{u}}{\partial t} + \mathcal{U} \cdot (\nabla \mathbf{u}) + \tau_{bf}\, \mathbf{u} + g \nabla \zeta - \mu \nabla \cdot \boldsymbol{\sigma}, \boldsymbol{\sigma} - \nabla \mathbf{u} \right) \right\|^2}{\left\| \left(\frac{\partial \zeta}{\partial t} + \mathcal{H} \nabla \cdot \mathbf{u}, \frac{\partial \mathbf{u}}{\partial t} + \mathcal{U} \cdot (\nabla \mathbf{u}) + \tau_{bf}\, \mathbf{u} + g \nabla \zeta - \mu \nabla \cdot \boldsymbol{\sigma}, \boldsymbol{\sigma} - \nabla \mathbf{u} \right) \right\|},$$

Thus:

$$\sup_{(v, \mathbf{w}, \mathbf{p}) \in V(\mathcal{P}_h^T) \setminus \{0\}} \frac{|B_{\mathrm{lin}}((\zeta, \mathbf{u}, \boldsymbol{\sigma}), (v, \mathbf{w}, \mathbf{p}))|}{\|(v, \mathbf{w}, \mathbf{p})\|} \geq \left\| \left(\frac{\partial \zeta}{\partial t} + \mathcal{H} \nabla \cdot (\mathbf{u}), \frac{\partial \mathbf{u}}{\partial t} + \mathcal{U} \cdot (\nabla \mathbf{u}) + \tau_{bf}\, \mathbf{u} + g \nabla \zeta - \mu \nabla \cdot \boldsymbol{\sigma}, \boldsymbol{\sigma} - \nabla \mathbf{u} \right) \right\|, \tag{13}$$

where the norm in the right hand side (RHS) is equivalent to the norm on $U(\Omega_{\mathrm{T}})$. We therefore conclude that the linearized weak formulation is well posed in this continuous functional setting.

In the spirit of the DPG method and to simplify the analysis of the AVS-FE weak formulation, we introduce an equivalent norm on the trial space, the energy norm $\|\cdot\|_{\mathrm{B}} : U(\Omega_{\mathrm{T}}) \longrightarrow [0, \infty)$:

$$\|(\zeta, \mathbf{u}, \boldsymbol{\sigma})\|_{\mathrm{B}} \stackrel{\mathrm{def}}{=} \sup_{(v,\mathbf{w},\mathbf{p})\in V(\mathcal{P}_h^T)\setminus\{0\}} \frac{|B_{\mathrm{lin}}((\zeta, \mathbf{u}, \boldsymbol{\sigma}),(v, \mathbf{w}, \mathbf{p}))|}{\|(v, \mathbf{w}, \mathbf{p})\|_{V(\mathcal{P}_h^T)}}. \tag{14}$$

Before proceeding to the FE discretization of the weak formulation (7), we point out that the weak formulation is well posed as it satisfies the *inf-sup* and continuity conditions in terms of the energy norm with an *inf-sup* constant of unity if we consider a linearized version of the SWE. Thus, the linearized form of this formulation satisfies the required conditions of the Babuška Lax-Milgram Theorem [4]. For an in-depth discussion on broken spaces and variational forms for the DPG method, we refer to [13]. We also define the optimal test functions $(\hat{e}, \hat{\boldsymbol{\varepsilon}}, \hat{\mathbf{E}}) \in V(\mathcal{P}_h^T)$, for each$(\zeta, \mathbf{u}, \boldsymbol{\sigma}) \in U(\Omega_{\mathrm{T}})$ as the solution of the Riesz representation problem:

$$\Big((\hat{e}, \hat{\boldsymbol{\varepsilon}}, \hat{\mathbf{E}}), (v, \mathbf{w}, \mathbf{p}) \Big)_{V(\mathcal{P}_h^T)} = B_{\mathrm{lin}}((\zeta, \mathbf{u}, \boldsymbol{\sigma}),(v, \mathbf{w}, \mathbf{p})), \quad \forall (v, \mathbf{w}, \mathbf{p}) \in V(\mathcal{P}_h^T). \tag{15}$$

This Riesz representation problem is well posed with unique solutions due to the inner product in the left hand side (LHS) and the continuity of the $B_{\mathrm{lin}}(\cdot, \cdot)$.

Using the FOSLS arguments to show the inf-sup condition (13) reveals the close relation between our method and the FOSLS. The two differ in the norm in which we perform the residual minimization process. In the corresponding FE discretization of (15), we will use an equivalent norm to the L^2 norm for discrete functions. Discrete well posedness is a direct consequence of the well-posedness of a FOSLS weak formulation. Approximation of the optimal test functions is necessary in this case due to our choice of norm since the optimal test functions cannot be explicitly established as is the case in FOSLS. Fortunately, since the test space is broken, the solution of (15) can be performed element wise, thereby removing the need for a global solve for the optimal test functions. We refer to the work of Storn [50] for further details on the relationship between the DPG and FOSLS.

While the definition of the energy norm makes the analysis of AVS-FE weak formulations straightforward, it is not computable as it is defined through a supremum. Thankfully, the definition of the optimal test functions through the Riesz representation problem ensures the following norm equivalence:

$$\|(\zeta, \mathbf{u}, \boldsymbol{\sigma})\|_{\mathrm{B}} = \left\|(\hat{e}, \hat{\boldsymbol{\varepsilon}}, \hat{\mathbf{E}})\right\|_{V(\mathcal{P}_h^T)}, \tag{16}$$

which is readily available for computations once the optimal test function $(\hat{e}, \hat{\boldsymbol{\varepsilon}}, \hat{\mathbf{E}})$ is known, see [12, 19] for details on optimal test functions and proof of the norm equivalence.

To establish FE approximations $(\zeta^h, \mathbf{u}^h, \boldsymbol{\sigma}^h)$ of $(\zeta, \mathbf{u}, \boldsymbol{\sigma})$, we make the standard FE choice of a finite dimensional subspace $U^h(\Omega_{\mathrm{T}}) \subset U(\Omega_{\mathrm{T}})$. Since $U(\Omega_{\mathrm{T}})$ consists of Hilbert spaces, we use classical FE basis functions, e.g., C^0 polynomials and/or Raviart-Thomas bases. Here, we make no particular choice other than using conforming approximation spaces. We subsequently use the Riesz problem (15) to establish an equivalent mixed problem where wee seek both the solution $(\zeta^h, \mathbf{u}^h, \boldsymbol{\sigma}^h)$ and a Riesz representer of the residual, $(\tilde{e}^h, \tilde{\boldsymbol{\varepsilon}}^h, \tilde{\mathbf{E}}^h)$:

$$\begin{aligned}
&\text{Find } (\zeta^h, \mathbf{u}^h, \boldsymbol{\sigma}^h) \in U^h(\Omega_{\mathrm{T}}), (\tilde{e}^h, \tilde{\boldsymbol{\varepsilon}}^h, \tilde{\mathbf{E}}^h) \in V^h(\mathcal{P}_h^T) && \text{such that:}\\
&\Big((\tilde{e}^h, \tilde{\boldsymbol{\varepsilon}}^h, \tilde{\mathbf{E}}^h), (v^h, \mathbf{w}^h, \mathbf{p}^h) \Big)_{V(\mathcal{P}_h^T)} - B((\zeta^h, \mathbf{u}^h, \boldsymbol{\sigma}^h); (v^h, \mathbf{w}^h, \mathbf{p}^h)) = -F(v^h, \mathbf{w}^h, \mathbf{p}^h) && \\
&\qquad \forall (v^h, \mathbf{w}^h, \mathbf{p}^h) \in V^h(\mathcal{P}_h^T), && \\
&B'((a^h, \mathbf{b}^h, \mathbf{c}^h), (\tilde{e}^h, \tilde{\boldsymbol{\varepsilon}}^h, \tilde{\mathbf{E}}^h)) = 0, && \\
&\qquad \forall\, (a^h, \mathbf{b}^h, \mathbf{c}^h) \in U^h(\Omega_{\mathrm{T}}). &&
\end{aligned} \tag{17}$$

The derivation of this system is based on the weak form (7), the Riesz representation problem (15), and the fact that the AVS-FE is a minimum residual method, see [22] and [11] for details on the derivation for linear and nonlinear problems, respectively. B' represents the Gateaux derivative of $B(\cdot; \cdot)$ form with respect to $(\zeta, \mathbf{u}, \boldsymbol{\sigma})$ acting on the approximation of the "error representation function" $(\tilde{e}, \tilde{\boldsymbol{\varepsilon}}, \tilde{\mathbf{E}})$, i.e., it represents a linearization of the differential operator $B(\cdot, \cdot)$. The mixed problem (17) is equivalent to a discrete version of the weak form (7) (see Theorem 2.2 of Carstensen et al. [11]). The linearization provided by the constraint equation on the Gateaux derivative B' allows

us to employ existing nonlinear FE solvers to perform iterations that (hopefully) converge to a stationary point. The inner product $(\cdot,\cdot)_{V(\mathcal{P}_h^T)}$ in (17) we use is similar to the one introduced in [10], however, we introduce weights to all derivative terms here:

$$\begin{aligned}((e,\boldsymbol{\varepsilon},\mathbf{E}),(v,\mathbf{w},\mathbf{p}))_{V(\mathcal{P}_h^T)} \overset{\text{def}}{=} \sum_{K_m\in\mathcal{P}_h^T}\int_{K_m}\Big[&h_m^2\nabla e_m\cdot\nabla v_m\\ &+e_m v_m+h_m^2\nabla\boldsymbol{\varepsilon}_m:\nabla\mathbf{w}_m+\boldsymbol{\varepsilon}_m\cdot\mathbf{w}_m\\ &+h_m^2(\nabla\cdot\mathbf{E}_m)(\nabla\cdot\mathbf{p}_m)+\mathbf{E}_m:\mathbf{p}_m\Big]\,\mathrm{d}\mathbf{x}.\end{aligned} \tag{18}$$

The induced norm is equivalent to the standard L^2 norm for discrete FE polynomials as we assume the mesh is quasi uniform such that standard inverse estimates are valid.

The error representation function $(\tilde{e}^h,\tilde{\boldsymbol{\varepsilon}}^h,\tilde{\mathbf{E}}^h)$ is a Riesz representer of the approximation error $(\zeta,\mathbf{u},\boldsymbol{\sigma})-(\zeta^h,\mathbf{u}^h,\boldsymbol{\sigma}^h)$ through an analogue of (15) where the RHS is the residual functional. Thus, due to the norm equivalence (16) the norm of the approximate error representation function is an *a posteriori* error estimate of the approximation error of the energy norm:

$$\left\|(\zeta-\zeta^h,\mathbf{u}-\mathbf{u}^h,\boldsymbol{\sigma}-\boldsymbol{\sigma}^h)\right\|_{\mathrm{B}}\approx\left\|(\tilde{e}^h,\tilde{\boldsymbol{\varepsilon}}^h,\tilde{\mathbf{E}}^h)\right\|_{V(\mathcal{P}_h^T)}. \tag{19}$$

This error estimate has been analyzed in [12] and its local restriction to an element is an error indicator:

$$\eta=\left\|(\tilde{e}^h,\tilde{\boldsymbol{\varepsilon}}^h,\tilde{\mathbf{E}}^h)\right\|_{V(K_m)}. \tag{20}$$

This error indicator has been successfully applied to a wide range of problems in both the DPG and AVS-FE methods [11, 13, 46, 52].

Remark 21 The size of the mixed discrete system of linear algebraic equations (17) is larger than the linear system corresponding to a direct discretization of (7) since we do not compute optimal test functions on the fly element-by-element. An advantage of this mixed form is that its solution immediately provides an a posteriori error estimate as well as error indicators to be used in mesh adaptive strategies. Furthermore, the structure of (17) allows straightforward implementation into high level FE solvers such as FEniCS [2].

Remark 22 The stability of (17) is unconditional in the "ideal" case in which we can exactly compute the error representation function. However, since this is not achievable in practical computations, we are forced to consider a practical implementation and consider an approximation of these functions [28]. Hence, this approximation leads to a potential loss of discrete stability it is not sufficiently accurate. In the DPG method, sufficient accuracy of the error representation function is guaranteed by the existence of (local) Fortin operators [8]. The construction of such operators is studied in great detail in [39], and its analysis was recently further refined in [21]. Generally, in DPG methods for linear second order PDEs, a Fortin operator's existence and thus discrete stability is ensured if the Riesz representation problems are solved using polynomials of order $r=p+\Delta p$, where p is the degree of the trial space discretization and $\Delta p=d$ the space dimension. However, while this enrichment degree ensures the existence of the required Fortin operator, numerical evidence suggest that in most cases $\Delta p=1$ is typically sufficient [21]. Alternative test spaces for the DPG method for singular perturbation problems are investigated in [47], even for the case of $\Delta p=0$. In the AVS-FE method, numerical evidence suggests that $r=p$ is sufficient [10] for convection-diffusion PDEs as well as extensive numerical experimentation for the SWE. Since the test functions are sought in a discontinuous polynomial space, using $r=p$ still results in a larger space than the trial as the discontinuous spaces contain additional degrees of freedom.

We also note that inspection of (17) and comparison to to the discretized weak forms in classical mixed methods (see, e.g., [9]) shows the close relation between these methods. The analysis of (17) can be borrowed from mixed methods. Hence, since the inner product satisfies a coercivity condition and if we replace $B(\cdot;\cdot)$ by $B_{\mathrm{lin}}(\cdot,\cdot)$ which satisfies a discrete *inf-sup* condition similar to (13), discrete stability of (17) follows.

2.3 Time slice approach

The numerical solution of the space-time discretizations (17) is akin to a FE discretization of a three dimensional problem thereby incurring a significant computational cost. To this end, we also introduce a "time-slice" approach as introduced for transient convection-diffusion in [24, 25] for the DPG method. While this can localize the overall computational cost of the space-time discretization, this approach can also be used to increase the accuracy in a similar fashion as for time-stepping approaches that gain accuracy as the time step size is reduced. Similar approaches were also employed in [3, 43, 44, 51] for the SWE for stabilized DG and streamlined-upwind Petrov-Galerkin (SUPG) methods.

We consider a partition of the domain Ω_T into space-time "slices", see Fig. 2 for an example in a spatially one dimensional domain. In each space-time slice, starting with the one intersecting the initial time boundary Ω_0, we solve the discrete space-time problem (17) as described in Section 2.2. Each successive slice is then solved by interpolating the previous solutions ζ^h_{prev}, $\mathbf{u}^h_{prev}$ at the final

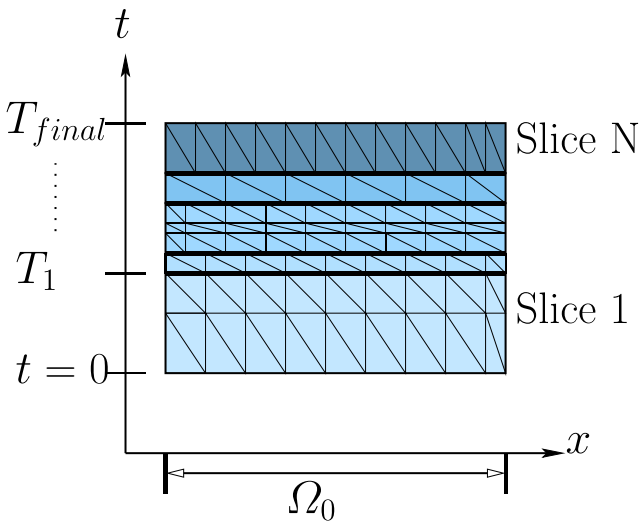

Fig. 2 Partition of a space-time domain into slices and finite elements

time of the previous slice onto the next as initial conditions. The slice configuration can be established in several ways, several of which are considered for the space-time DPG method in [24, 25]. Furthermore, the built-in error estimator and error indicators of the AVS-FE method lets us perform space-time mesh adaptive refinements on each individual slice. Note that in the case of local space-time mesh refinements on each slice, the slice itself is fixed whereas the mesh is refined. Such local refinements are of particular interest in applications where the solution response varies greatly in time, thereby allowing us to adaptively refine the mesh to the required resolution in each slice. This is shown in Fig. 2 with variable thickness of the slices in the t direction.

3 A priori error analysis

Here, we present *a priori* error estimates for the full space-time AVS-FE approximations for the SWE in terms of appropriate norms of the approximation error. Due to the energy norm (14) and the best approximation error of the AVS-FE method in terms of this norm, the following proofs rely on classical bounds in Hilbert spaces for continuous and discontinuous FE approximation functions. In the analysis we assume that the elevation and velocity trial variables are discretized using classical C^0 continuous FE polynomial basis functions, whereas $\boldsymbol{\sigma}^h$ is discretized using Raviart-Thomas bases. Other alternatives for $\boldsymbol{\sigma}^h$ such as Brezzi-Douglas-Marini basis functions can also be employed with minor modifications to the following analyses and we refer to the text by Brezzi and Fortin [9] for details. We also assume that we are considering a linearized version of the SWE.

Remark 31 We do not present an analysis of the nonlinear convergence properties for the SWE here but refer interested readers to chapter 8 of the text by Bochev and Gunzberger [7] where a highly detailed analysis and error estimates of the FOSLS for the closely related Navier-Stokes equations are presented using a fixed point theorem.

First, we introduce the best and quasi-best approximation properties of the AVS-FE method to facilitate proofs of the *a priori* bounds which are to follow.

Proposition 31 *Let* $(\zeta, \mathbf{u}, \boldsymbol{\sigma}) \in U(\Omega_T)$ *be the exact solution of the AVS-FE weak formulation* (7) *and* $(\zeta^h, \mathbf{u}^h, \boldsymbol{\sigma}^h) \in U^h(\Omega_T)$ *its corresponding AVS-FE approximation from* (17)*. Then:*

$$\begin{aligned} &\left\|(\zeta - \zeta^h, \mathbf{u} - \mathbf{u}^h, \boldsymbol{\sigma} - \boldsymbol{\sigma}^h)\right\|_B \\ &\qquad \leq \left\|(\zeta - v^h, \mathbf{u} - \mathbf{w}^h, \boldsymbol{\sigma} - \mathbf{p}^h)\right\|_B . \end{aligned} \tag{21}$$

Proof The definition of the energy norm (14) gives:

$$\begin{aligned} &\left\|(\zeta - \zeta^h, \mathbf{u} - \mathbf{u}^h, \boldsymbol{\sigma} - \boldsymbol{\sigma}^h)\right\|_{\mathrm{B}} \\ &= \sup_{(v^h, \mathbf{w}^h, \mathbf{p}^h) \in V(\mathcal{P}_h^T)\setminus\{0\}} \frac{|B_{\mathrm{lin}}((\zeta - \zeta^h, \mathbf{u} - \mathbf{u}^h, \boldsymbol{\sigma} - \boldsymbol{\sigma}^h), (v^h, \mathbf{w}^h, \mathbf{p}^h))|}{\left\|(v^h, \mathbf{w}^h, \mathbf{p}^h)\right\|_{V(\mathcal{P}_h^T)}}, \end{aligned}$$

we use the standard trick and add $v^h - v^h$, $\mathbf{w}^h - \mathbf{w}^h$, $\mathbf{p}^h - \mathbf{p}^h$ to the trial functions. Then, linearity of $B(\cdot, \cdot)$ in its first argument and Galerkin orthogonality yield:

$$\begin{aligned} &\left\|(\zeta - \zeta^h, \mathbf{u} - \mathbf{u}^h, \boldsymbol{\sigma} - \boldsymbol{\sigma}^h)\right\|_{\mathrm{B}} \\ &= \sup_{(v^h, \mathbf{w}^h, \mathbf{p}^h) \in V(\mathcal{P}_h^T)\setminus\{0\}} \frac{|B_{\mathrm{lin}}((\zeta - v^h, \mathbf{u} - \mathbf{w}^h, \boldsymbol{\sigma} - \mathbf{p}^h), (v^h, \mathbf{w}^h, \mathbf{p}^h))|}{\left\|(v^h, \mathbf{w}^h, \mathbf{p}^h)\right\|_{V(\mathcal{P}_h^T)}}, \end{aligned}$$

continuity of $B_{\mathrm{lin}}(\cdot, \cdot)$ with its continuity constant of 1 in the energy norm completes the proof. □

Since the energy norm is an equivalent norm on $U(\Omega_{\mathrm{T}})$, we also have the quasi-best approximation property:

$$\begin{aligned} &\left\|(\zeta - \zeta^h, \mathbf{u} - \mathbf{u}^h, \boldsymbol{\sigma} - \boldsymbol{\sigma}^h)\right\|_{U(\Omega_{\mathrm{T}})} \\ &\leq C \left\|(\zeta - v^h, \mathbf{u} - \mathbf{w}^h, \boldsymbol{\sigma} - \mathbf{p}^h)\right\|_{U(\Omega_{\mathrm{T}})}, \end{aligned} \tag{22}$$

where the constant C is independent of the mesh and depends on norm equivalence constants between the energy norm and $\|\cdot\|_{U(\Omega_{\mathrm{T}})}$ as well as the continuity constant of a Fortin operator (see Remark 22). Note that we assume quasi uniform such that we have inverse estimates ensuring the equivalence of the L^2 norm and $\|\cdot\|_{V(\mathcal{P}_h^T)}$.

Another key component in the following analysis is the convergence of polynomial interpolating functions. Hence, there exist a polynomial interpolation operator Π_{hp} [5]:

$$\Pi_{hp} : U \to U^{hp}. \tag{23}$$

Thus, $\Pi_{hp}(u)$ represents an interpolant of u consisting of continuous polynomials, then [40]:

Theorem 31 *Let $u \in H^r(\Omega)$ and $\Pi_{hp}(u) \in U^{hp}$ be the interpolant of u (23). Then, there exists $C > 0$ such that the interpolation error can be bounded as follows:*

$$\left\| u - \Pi_{hp}(u) \right\|_{H^s(\Omega)} \leq C \frac{h^{\mu - s}}{p^{r-s}} \left\| u \right\|_{H^r(\Omega)}, \tag{24}$$

where h is the maximum element diameter, p the minimum polynomial degree of interpolants in the mesh, $s \leq r$, and $\mu = min\ (p+1, r)$.

Second, we have the interpolation operator for Raviart-Thomas [9] spaces, ρ_{hp}:

$$\rho_{hp} : Q \rightarrow Q^{hp}, \tag{25}$$

Thus, $\rho_{hp}(\mathbf{q})$ represents an interpolant of $\mathbf{q}$ consisting of polynomials which **normal** components are continuous, then [9]:

Theorem 32 *Let $\mathbf{q} \in H(\boldsymbol{div}, \Omega)$ and $\rho_{hp}(\mathbf{q}) \in Q^{hp}$ be the interpolant of $\mathbf{q}$ (25). Then, there exists $C > 0$ such that the interpolation error can be bounded as follows:*

$$\exists\, C > 0 : \left\| \mathbf{q} - \rho_{hp}(\mathbf{q}) \right\|_{H(\boldsymbol{div}, \Omega)} \leq C\, h^n |\mathbf{q}|_{H^{n+1}(\Omega)}, \tag{26}$$

where h is the maximum element diameter and n the minimum order of Raviart-Thomas interpolants in the mesh.

The final point we highlight before proceeding with the main results of this section are on the convergence properties of interpolants of piecewise discontinuous polynomials. In [45] Riviére et al. present a result analogous to Theorem 31 for polynomial interpolants in broken Hilbert spaces.

The first *a priori* bound we present is in terms of the energy norm. While not exactly computable, it is natural to present as the energy norm is central to the stability of our method. Furthermore, we can approximate the error in the energy norm through (19).

Lemma 31 *Let $(\zeta, \mathbf{u}, \boldsymbol{\sigma}) \in U(\Omega_T)$ be the exact solution of the AVS-FE weak formulation (7) and $(\zeta^h, \mathbf{u}^h, \boldsymbol{\sigma}^h) \in U^h(\Omega_T)$ its corresponding AVS-FE approximation from (17). Then:*

$$\left\| (\zeta - \zeta^h, \mathbf{u} - \mathbf{u}^h, \boldsymbol{\sigma} - \boldsymbol{\sigma}^h) \right\|_B \leq C \frac{h^{\mu - 1}}{p_{\mathbf{u}}^{r-1}}, \tag{27}$$

where h is the maximum element diameter, $\mu = min\ (p_{\mathbf{u}} + 1, r)$, $p_{\mathbf{u}}$ the minimum polynomial degree of approximation of $\mathbf{u}^h$ and ζ^h in the mesh, and r the minimum regularity of either of the solution components $(\hat{e}, \hat{\boldsymbol{\varepsilon}}, \hat{\mathbf{E}})$ of the distributional PDE underlying the Riesz representation problem (15).

Proof The RHS of (21) can be bounded by the error in the Riesz representers of the exact and approximate AVS-FE trial functions by the energy norm equivalence in (16), and the map induced by the Riesz representation problem (15) to yield:

$$\left\| (\zeta - \zeta^h, \mathbf{u} - \mathbf{u}^h, \boldsymbol{\sigma} - \boldsymbol{\sigma}^h) \right\|_{\mathrm{B}} \leq C \left\| (\hat{e} - \hat{e}^h, \hat{\boldsymbol{\varepsilon}} - \hat{\boldsymbol{\varepsilon}}^h, \hat{\mathbf{E}} - \hat{\mathbf{E}}^h) \right\|_{V(\mathcal{P}_h^T)},$$

where $(\hat{e}, \hat{\boldsymbol{\varepsilon}}, \hat{\mathbf{E}}) \in V(\mathcal{P}_h^T)$ are the exact Riesz representers of $(\zeta, \mathbf{u}, \boldsymbol{\sigma})$ through (15), and $(\hat{e}^h, \hat{\boldsymbol{\varepsilon}}^h, \hat{\mathbf{E}}^h) \in V^*(\mathcal{P}_h^T)$ are the approximate Riesz representers of $(\zeta^h, \mathbf{u}^h, \boldsymbol{\sigma}^h)$ through a FE discretization of (15). The definition of the norm $\|\cdot\|_{V(\mathcal{P}_h^T)}$ induced by the inner product in (18) then gives:

$$\begin{aligned} \left\| (\zeta - \zeta^h, \mathbf{u} - \mathbf{u}^h, \boldsymbol{\sigma} - \boldsymbol{\sigma}^h) \right\|_{\mathrm{B}} \leq C \Bigg\{ & \sum_{K_m \in \mathcal{P}_h^T} h_m \left\| \nabla \hat{e} - \nabla \hat{e}^h \right\|_{L^2(K_m)} + \sum_{K_m \in \mathcal{P}_h^T} h_m \left\| \nabla \hat{\mathbf{E}} - \nabla \hat{\mathbf{E}}^h \right\|_{L^2(K_m)} \\ & + \sum_{K_m \in \mathcal{P}_h^T} h_m \left\| \nabla \cdot \hat{\boldsymbol{\varepsilon}} - \nabla \cdot \hat{\boldsymbol{\varepsilon}}^h \right\|_{L^2(K_m)} + \left\| \hat{e} - \hat{e}^h \right\|_{L^2(\Omega_{\mathrm{T}})} + \left\| \hat{\mathbf{E}} - \hat{\mathbf{E}}^h \right\|_{L^2(\Omega_{\mathrm{T}})} + \left\| \hat{\boldsymbol{\varepsilon}} - \hat{\boldsymbol{\varepsilon}}^h \right\|_{L^2(\Omega_{\mathrm{T}})} \Bigg\}. \end{aligned}$$

Since the L^2 and seminorms are bounded by the H^1 norm, and we pick $h_m = h$:

$$\begin{aligned} \left\| (\zeta - \zeta^h, \mathbf{u} - \mathbf{u}^h, \boldsymbol{\sigma} - \boldsymbol{\sigma}^h) \right\|_{\mathrm{B}} \leq C \Bigg\{ & \left\| \hat{e} - \hat{e}^h \right\|_{H^1(\mathcal{P}_h^T)} + \left\| \hat{\boldsymbol{\varepsilon}} - \hat{\boldsymbol{\varepsilon}}^h \right\|_{H^1(\mathcal{P}_h^T)} + \left\| \hat{\mathbf{E}} - \hat{\mathbf{E}}^h \right\|_{H^1(\mathcal{P}_h^T)} \\ & + h \left\| \hat{e} - \hat{e}^h \right\|_{H^1(\mathcal{P}_h^T)} + h \left\| \hat{\boldsymbol{\varepsilon}} - \hat{\boldsymbol{\varepsilon}}^h \right\|_{H^1(\mathcal{P}_h^T)} + h \left\| \hat{\mathbf{E}} - \hat{\mathbf{E}}^h \right\|_{H^1(\mathcal{P}_h^T)} \Bigg\}. \end{aligned}$$

Next, we apply the bounds in [45]:

$$\left\|(\zeta-\zeta^h,\mathbf{u}-\mathbf{u}^h,\boldsymbol{\sigma}-\boldsymbol{\sigma}^h)\right\|_{\mathrm{B}} \leq C(1+h) \times\left\{\frac{h^{\mu_{\hat{e}}-1}}{p_{\hat{e}}^{r_{\hat{e}}-1}}+\frac{h^{\mu_{\hat{\boldsymbol{\varepsilon}}}-1}}{p_{\hat{\boldsymbol{\varepsilon}}}^{r_{\hat{\boldsymbol{\varepsilon}}}-1}}+\frac{h^{\mu_{\hat{\mathbf{E}}}-1}}{p_{\hat{\mathbf{E}}}^{r_{\hat{\mathbf{E}}}-1}}\right\},$$

where $\mu_i = \min(p_i+1, r_i)$, r_i the regularity of the solution of the underlying distributional PDE and i denote the components $(\hat{e}, \hat{\boldsymbol{\varepsilon}}, \hat{\mathbf{E}})$. Finally, we complete the proof by noting that we that we pick the same degree p for all variables and that the term with the smallest r will dominate the error. Hence, we get the desired bound (27). □

Second, we establish a bounds in terms of the Sobolev Norm $\|\cdot\|_{U(\Omega_{\mathrm{T}})}$.

Lemma 32 *Let* $(\zeta,\mathbf{u},\boldsymbol{\sigma}) \in U(\Omega_T)$ *be the exact solution of the AVS-FE weak formulation* (7) *and* $(\zeta^h,\mathbf{u}^h,\boldsymbol{\sigma}^h) \in U^h(\Omega_T)$ *its corresponding AVS-FE approximation from* (17)*. Then:*

$$\left\|(\zeta-\zeta^h,\mathbf{u}-\mathbf{u}^h,\boldsymbol{\sigma}-\boldsymbol{\sigma}^h)\right\|_{U(\Omega_T)} \leq C\left\{\frac{h^{\mu-1}}{p^{r-1}}+h^n\right\}, \tag{28}$$

where h *is the maximum element diameter,* $\mu = min\,(p+1, r)$*,* p *the minimum polynomial degree of approximation of* $\mathbf{u}^h$ *and* ζ^h *in the mesh,* r *the minimum regularity of the solution components* $\mathbf{u}$ *and* ζ *of the underlying distributional SWE PDEs, and* $n = p_{\mathbf{u}} - 1$ *the minimum order of the Raviart-Thomas elements in the mesh.*

Proof By the quasi-best approximation property (22):

$$\left\|(\zeta-\zeta^h,\mathbf{u}-\mathbf{u}^h,\boldsymbol{\sigma}-\boldsymbol{\sigma}^h)\right\|_{U(\Omega_{\mathrm{T}})} \leq C\left\|(\zeta-v^h,\mathbf{u}-\mathbf{w}^h,\boldsymbol{\sigma}-\mathbf{p}^h)\right\|_{U(\Omega_{\mathrm{T}})},$$

the definition of the norm on $U(\Omega_{\mathrm{T}})$ (10) leads to:

$$\left\|(\zeta-\zeta^h,\mathbf{u}-\mathbf{u}^h,\boldsymbol{\sigma}-\boldsymbol{\sigma}^h)\right\|_{U(\Omega_{\mathrm{T}})} \leq C\left\{\left\|\zeta-v^h\right\|_{H^1(\Omega_{\mathrm{T}})}+\left\|\mathbf{u}-\mathbf{w}^h\right\|_{H^1(\Omega_{\mathrm{T}})}+\left\|\boldsymbol{\sigma}-\mathbf{p}^h\right\|_{H(\mathbf{div},\Omega)}\right\}.$$

An application of Theorem 31 with $s = 1$ and Theorem 32 then gives:

$$\left\|(\zeta-\zeta^h,\mathbf{u}-\mathbf{u}^h,\boldsymbol{\sigma}-\boldsymbol{\sigma}^h)\right\|_{U(\Omega_{\mathrm{T}})} \leq C\left\{\frac{h^{\mu_\zeta-1}}{p_\zeta^{r-1}}+\frac{h^{\mu_{\mathbf{u}}-1}}{p_{\mathbf{u}}^{r-1}}+h^n\right\}.$$

In the AVS-FE method, we always pick $p_{\mathbf{u}} = p_\zeta$, then considering only the largest of the fractions, the bound (28) follows and the proof is complete. □

Remark 32 To conclude this section, we make an important remark on the AVS-FE approximations for the variable $\boldsymbol{\sigma}^h$. For convex domains Ω_T and smooth sources $\mathbf{f}$, the regularity of $\boldsymbol{\sigma}$ is higher than the $H(\mathbf{div},\Omega)$ dictated by the weak form (7), i.e., $H^1(\Omega)$. Thus, it is appropriate to use C^0 continuous basis functions as advocated in [10]. As the application of the SWE often in complex coastal domains which are irregular, users of this method should use $H(\mathbf{div},\Omega)$ conforming approximations such as Raviart-Thomas elements as a general rule-of-thumb in coastal domains. As in [9], the minimum order of the Raviart-Thomas elements is one order below the polynomial order for the approximate velocity. Hence, increasing the order of these elements above this does not increase the accuracy as the bounds on $\boldsymbol{\sigma}-\boldsymbol{\sigma}^h$ depend on the order of the velocity approximations.

4 Numerical verifications

In this section, we present numerical verifications for the AVS-FE method and the SWE. First, we consider several academic problems to ascertain convergence behavior under both uniform and adaptive mesh refinements. Finally, we consider a series of common physical benchmark problems for shallow water models from literature. While the *a priori* error estimates are established based on a linearized SWE, we consider only the full nonlinear case here as a linear SWE is generally not appropriate in physical applications of interest. For all verifications, we solve the saddle point system (17). All numerical experiments presented here are performed using the FE solver FEniCS [2]. To converge to the nonlinear SWE solutions, we employ the Portable, Extensible Toolkit for Scientific Computation (PETSc) library Scalable Nonlinear Equations Solvers (SNES) [1, 6] to perform Newton iterations within FEniCS. To minimize the errors of these iterations, we set the nonlinear convergence tolerance to the value 10^{-14}. Based on our experience this typically leads to a converged solution in less than 6 nonlinear iterations with an initial guess of a zero solution.

4.1 Numerical asymptotic convergence studies

To present the convergence properties of the AVS-FE method applied to the SWE, we consider a case where the bathymetry is assumed to be constant equal to zero, i.e., $H = \zeta$. We consider a case in which the exact elevation is:

$$\zeta_{ex} = \cos(x+y-t), \tag{29}$$

whereas the components of the velocity vector $\mathbf{u}_{ex}$ are both:

$$u_{ex} = \sin(x+y+t). \tag{30}$$

The other parameters we pick are $\mu = 10^{-5}$ and $\tau_{bf} = 1$, the spatial domain is the unit square, with Γ_{I} the line segment at $x = 0$, and the temporal domain is from $t = 0$ to $t = 0.5$. The exact solutions are then used to establish proper boundary conditions and source terms for the SWE. In the FE approximation, we employ Lagrange bases for ζ^h, $\mathbf{u}^h$, and $\boldsymbol{\sigma}^h$ since in this case the smooth solutions make C^0 regularity an appropriate choice for discretization of $H(\mathbf{div}, \Omega)$. Since we solve (17), we also need to specify functions spaces for the error representation function, in this case we pick discontinuous Lagrange polynomials for all components of this space of the same polynomial degree as the velocity. Hence, the discrete spaces are:

$$\begin{aligned} U^h(\Omega_{\mathrm{T}}) &= \mathcal{P}^p(\Omega_T) \times [\mathcal{P}^p(\Omega_T)]^2 \times [\mathcal{P}^{p-1}(\Omega_T)]^4, \\ V^h(\mathcal{P}_h^T) &= \mathcal{P}^p(\mathcal{P}_h^T) \times [\mathcal{P}^p(\mathcal{P}_h^T)]^2 \times [\mathcal{P}^p(\mathcal{P}_h^T)]^4. \end{aligned} \tag{31}$$

Here $\mathcal{P}^p(\Omega_T)$ and $\mathcal{P}^p(\mathcal{P}_h^T)$ denote the space of continuous polynomials on Ω_T and discontinuous polynomials on $\mathcal{P}_h^T$, respectively.The initial mesh consists of six tetrahedron elements to which we perform uniform mesh refinements to ascertain the asymptotic convergence rates of applicable norms of the numerical approximation errors.

In Fig. 3, we present the convergence results in several error norms, with the observed rates of convergence listed in Table 1. The rates of the energy norm and $\|\cdot\|_{U(\Omega_{\mathrm{T}})}$ are as expected by the *a priori* estimates of Section 3. Also note that the rates of the individual error norms are of the same order as their underlying polynomial interpolants. We also point out that the error in the energy norm converges at a higher rate than $\left\|\boldsymbol{\sigma} - \boldsymbol{\sigma}^h\right\|_{H(\mathbf{div},\Omega)}$. Inspection of Lemma 31 reveals that the error in the energy norm does not depend on the order of the approximations used for $\boldsymbol{\sigma}^h$ but rather the polynomial degree of the error representation function.

Table 1 Error convergence rates corresponding to Fig. 3

Norm	Observed rate
$\left\|\zeta - \zeta^h\right\|_{L^2(\Omega_{\mathrm{T}})}$	3
$\left\|\mathbf{u} - \mathbf{u}^h\right\|_{L^2(\Omega_{\mathrm{T}})}$	3
$\left\|\boldsymbol{\sigma} - \boldsymbol{\sigma}^h\right\|_{L^2(\Omega_{\mathrm{T}})}$	2
$\left\|(\zeta - \zeta^h, \mathbf{u} - \mathbf{u}^h, \boldsymbol{\sigma} - \boldsymbol{\sigma}^h)\right\|_{L^2(\Omega_{\mathrm{T}})}$	2
$\left\|\zeta - \zeta^h\right\|_{H^1(\Omega_{\mathrm{T}})}$	2
$\left\|\mathbf{u} - \mathbf{u}^h\right\|_{H^1(\Omega_{\mathrm{T}})}$	2
$\left\|\boldsymbol{\sigma} - \boldsymbol{\sigma}^h\right\|_{H(\mathbf{div},\Omega)}$	1
$\left\|(\zeta - \zeta^h, \mathbf{u} - \mathbf{u}^h, \boldsymbol{\sigma} - \boldsymbol{\sigma}^h)\right\|_{U(\Omega_{\mathrm{T}})}$	1
$\left\|(\zeta - \zeta^h, \mathbf{u} - \mathbf{u}^h, \boldsymbol{\sigma} - \boldsymbol{\sigma}^h)\right\|_{\mathrm{B}}$	2

4.2 Adaptive mesh refinement

In this section, we present numerical verifications for space-time adaptive mesh refinement. We employ the built-in error indicators of the AVS-FE method (20) and the adaptive strategy of Dörfler [23] with the parameter $\theta = 0.35$.

We consider the limiting case for the SWE of purely convective flow. Hence, we set $\mu = 0$, $\tau_{bf} = 1$, the final time $T = 0.5$, and we consider exact solutions inspired by [46]:

$$\begin{aligned} \zeta^{ex}(\mathbf{x}, t) &= e^{-0.1t}\, e^{2\lambda x}, \\ u_x^{ex}(\mathbf{x}, t) &= e^{-0.1t} \left(x + \frac{e^{50x} - 1}{1 - e^{50}} \right) (1 - e^{\lambda x} \sin(2\pi y)), \\ u_y^{ex}(\mathbf{x}, t) &= e^{-0.1t} \left(x + \frac{e^{50x} - 1}{1 - e^{50}} \right) \frac{\lambda}{2\pi}\, e^{\lambda x} \sin(2\pi y), \end{aligned} \tag{32}$$

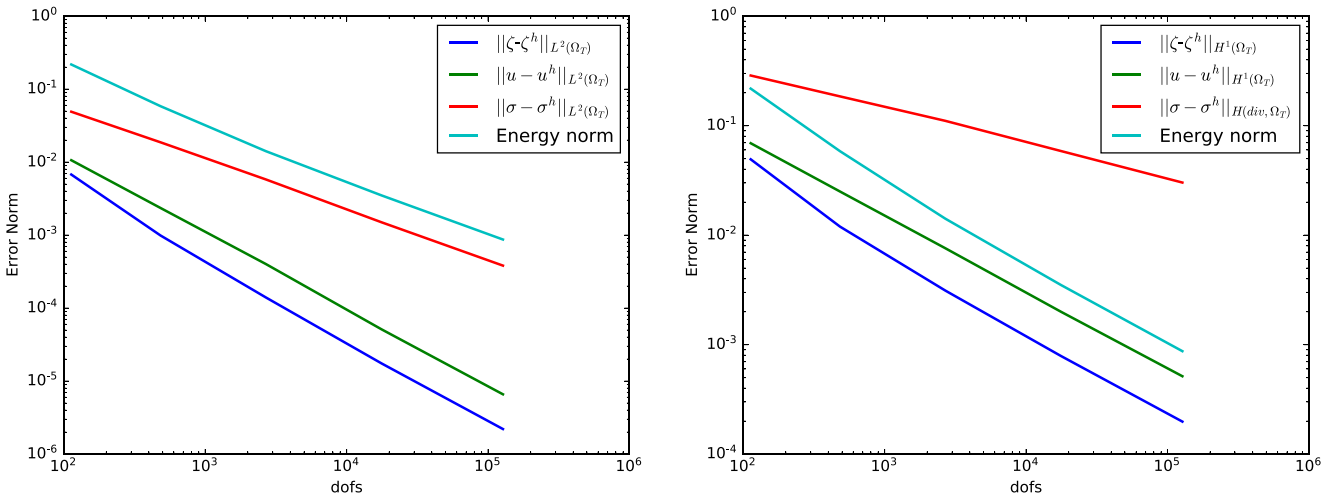

(a) $L^2(\Omega_{\mathrm{T}})$ and Energy error norms.

(b) $H^1(\Omega_{\mathrm{T}})$, $H(\mathbf{div}, \Omega)$ and Energy error norms.

Fig. 3 Error convergence results for uniform h-refinements for the SWE using polynomial approximations that are quadratic for ζ^h, $\mathbf{u}^h$ and linear for $\boldsymbol{\sigma}^h$

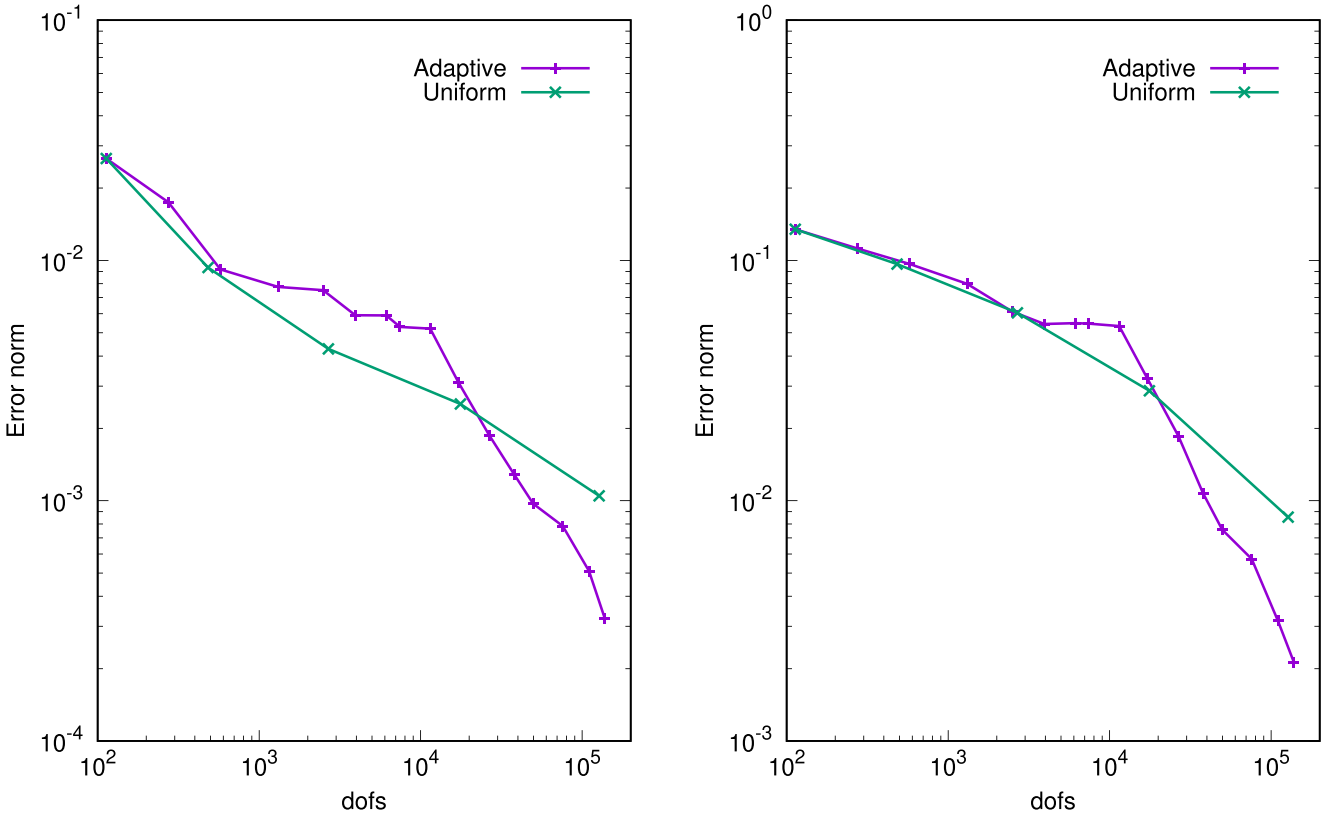

(a) $\|\zeta - \zeta^h\|_{L^2(\Omega_T)}$. (b) $\|\mathbf{u} - \mathbf{u}^h\|_{L^2(\Omega_T)}$.

Fig. 4 Comparison of error convergence for uniform and adaptive h-refinements in the full space-time domain

where the parameter λ is chosen to be $5 - \sqrt{25+4\pi^2}$. The initial mesh consists of six space-time tetrahedrons using quadratic polynomial basis functions for ζ^h, $\mathbf{u}^h$, linear polynomials for $\boldsymbol{\sigma}^h$, (see (31) for the definition of the discrete function spaces) and discontinuous quadratic polynomial bases for the components of the error representation function. We perform a total of five refinements for the uniform case and 16 for the adaptive case. We report the convergence histories in Fig. 4 comparing uniform and adaptive refinements. For the adaptive case, the asymptotic range of convergence is attained at approximately 10^4 degrees of freedom as indicated by the increased slope. On the other hand, the uniform refinements fail to reach the asymptotic region of convergence in this case.

4.3 Time slice approach

Next, we consider a verification of the time slice approach introduced in Section 2.3, we again consider the exact solution given in (29) and (30), $\mu = 10^{-5}$, $\tau_{bf} = 1$, and a final time of $4s$. To compare the full space-time and the space-time slices, we solve the problem using both approaches employing adaptive mesh refinements according to the built-in error indicators (20) and the same marking strategy as in the preceding verification. For the full space-time method, the initial mesh consists of 12 tetrahedron elements whereas for the time slice approach, we partition the space-time domain into eight equal slices discretized using 12 tetrahedron elements. Note that the space-time slices are kept fixed and we perform refinements that are local to each slice only. In both cases, we use quadratic polynomial basis functions for ζ^h, $\mathbf{u}^h$, linear polynomials for $\boldsymbol{\sigma}^h$, discontinuous quadratic polynomial bases for the error representation function, and perform a total of 12 mesh refinements in the full space-time domain, and on each slice individually, respectively. Hence, all function spaces are as defined in (31) with $p = 2$ (Fig. 5).

The comparison of the computational cost of these two approaches is not straightforward since the distribution of the computational cost is quite different. Here, we elect to present a comparison of error norms versus the number of degrees of freedom of the full space-time approach with the maximum number of maximum number of degrees of freedom at each level of refinement across all eight slices as

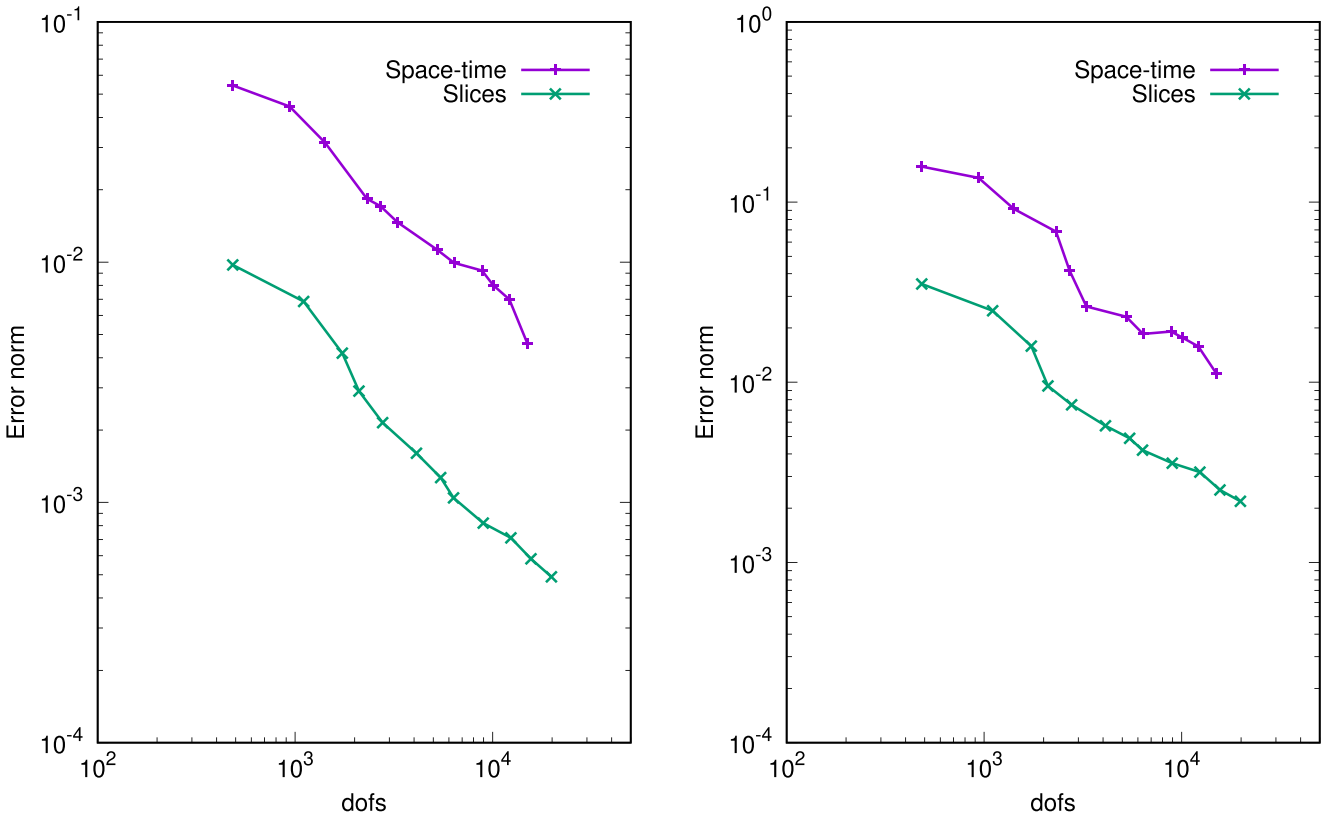

(a) $\|\zeta - \zeta^h\|_{L^2(\Omega_T)}$. (b) $\|\mathbf{u} - \mathbf{u}^h\|_{L^2(\Omega_T)}$.

Fig. 5 Error convergence results comparing the space-time and time slice approaches

well as the overall CPU times for both approaches. The first approach is selected as the largest cost in these computations is the inversion of the stiffness matrices. Inspection of Figs. 6 and 5 shows that in this case, the time slice approach is nearly an order of magnitude more accurate for the L^2 errors in ζ and $\mathbf{u}$. We have observed that for problems where the final time is less than one second, the two approaches yield essentially the same accuracy. However, as this example shows, once the final time becomes larger, the time slice approach is superior in terms of accuracy. However, in terms of computational time, the full-space time approach is roughly an order of magnitude faster ($\sim 300s$ versus $\sim 2000s$).

To show the converse, we again consider exactly the same problem with only five mesh refinements on each individual slice. In this case, the time slice approach is roughly 30% faster ($\sim 200s$ versus $\sim 300s$) and is more accurate as shown in Fig. 7. For this case we only show the L^2 errors in ζ and $\mathbf{u}$ and note that the other norms show identical trends.

4.4 Lake at rest

In cases of variable bathymetry $h_b(\mathbf{x})$, a common concern in the approximation of the SWE is the ability to preserve the steady state of a lake at rest throughout the time stepping procedure. Numerical approximations that preserve this steady state are referred to as being well balanced [33, 37]. We consider a two-dimensional case $\Omega = (0, 1m) \times (0, 1m)$, with physical parameters $\mu = 10^{-5}m$ and $\tau_b = 1s^{-1}$, and boundary conditions:

$$\begin{aligned} \zeta_0 &= 0, \\ u_0 &= 0, \\ u &= 0, \text{ on } \partial\Omega, \\ \zeta &= 1m, \text{ on } \partial\Omega. \end{aligned} \tag{33}$$

Consequently, there are no sources to induce flow in this example. The bathymetry is $h_b(\mathbf{x}) = 2m - h_0(\mathbf{x})$, where h_0 is given in (34). The final time is set to $10s$, and, the discrete function spaces used are as defined in (31) with $p = 2$. We consider a space-time mesh partition consisting of 150 space-time tetrahedrons such that the "width" of the elements in the time direction are equal to $10s$. The resulting errors in elevation and velocity are shown in Table 2. The L^2 errors are vanishingly small, leading us to conclude that this scheme is well balanced.

$$h_0(\mathbf{x}) = \begin{cases} 62.5\frac{1}{m^3}(x-0.3m)(x-0.7m)(y-0.3m)(y-0.7), & \text{if } (0.3m < x < 0.7m) \wedge (0.3m < y < 0.7m) \\ 0, & \text{otherwise} \end{cases}. \tag{34}$$

4.5 Tidal fluctuations

An important source impacting the flows governed by the SWE are tidal forces, as hurricane storm surge can be greatly increased by tidal fluctuations. Hence, it is critical that the AVS-FE approximations of the SWE are able to accurately reproduce phenomena corresponding to tidal fluctuations. To this end, we consider a model problem from [15] to facilitate comparison with existing FE methods for the SWE. The spatial domain is a one-dimensional channel $\Omega = (x_L, x_R) = (0, 10000m)$ with a constant bathymetry $h_b(\mathbf{x}) = 10m$, the physical parameters are $\mu = 25m$, $\tau_b = 0.01s^{-1}$, and the initial and boundary conditions are:

$$\begin{aligned} &\zeta_0 = 0, \\ &u_0 = 0, \\ &\boldsymbol{\sigma}(0,t) = 0, \\ &u(10000m,t) = 0, \\ &\zeta(0,t) = 0.1\cos(t\alpha)\, m, \end{aligned} \tag{35}$$

where $\alpha = 0.00014051891708$. Since this is a one-dimensional problem, the spaces $H(\mathbf{div}, \Omega)$ and $H^1(\Omega)$ coincide and we use C^0 polynomial approximations for all trial variables as defined in (31) with $p = 2$. As the period of tidal fluctuations are of order days, we consider a case in which the fluctuations occur over 7 days, i.e., the space-time domain is $\Omega_{\mathrm{T}} = (0, 10000m) \times (0, 604800s)$. In the AVS-FE discretization of the space-time domain we employ a uniform mesh of $2(25 \times 400)$ triangular elements, which corresponds to a "time step" of 1512 seconds.

In Fig. 8, the water column elevation at $x = 800m$ is shown for the full 7 day time span. As expected, the resulting tidal fluctuation leads to a sinusoidal elevation profile and at $x = 800m$, the wave amplitude is slightly damped from the incoming tidal wave. Correspondingly, in Fig. 9, the corresponding velocity is presented. Here we observe that the highest velocity magnitudes occur slightly before and after the peak tidal elevation. Visual inspection of the results in [15] shows comparable behavior with the

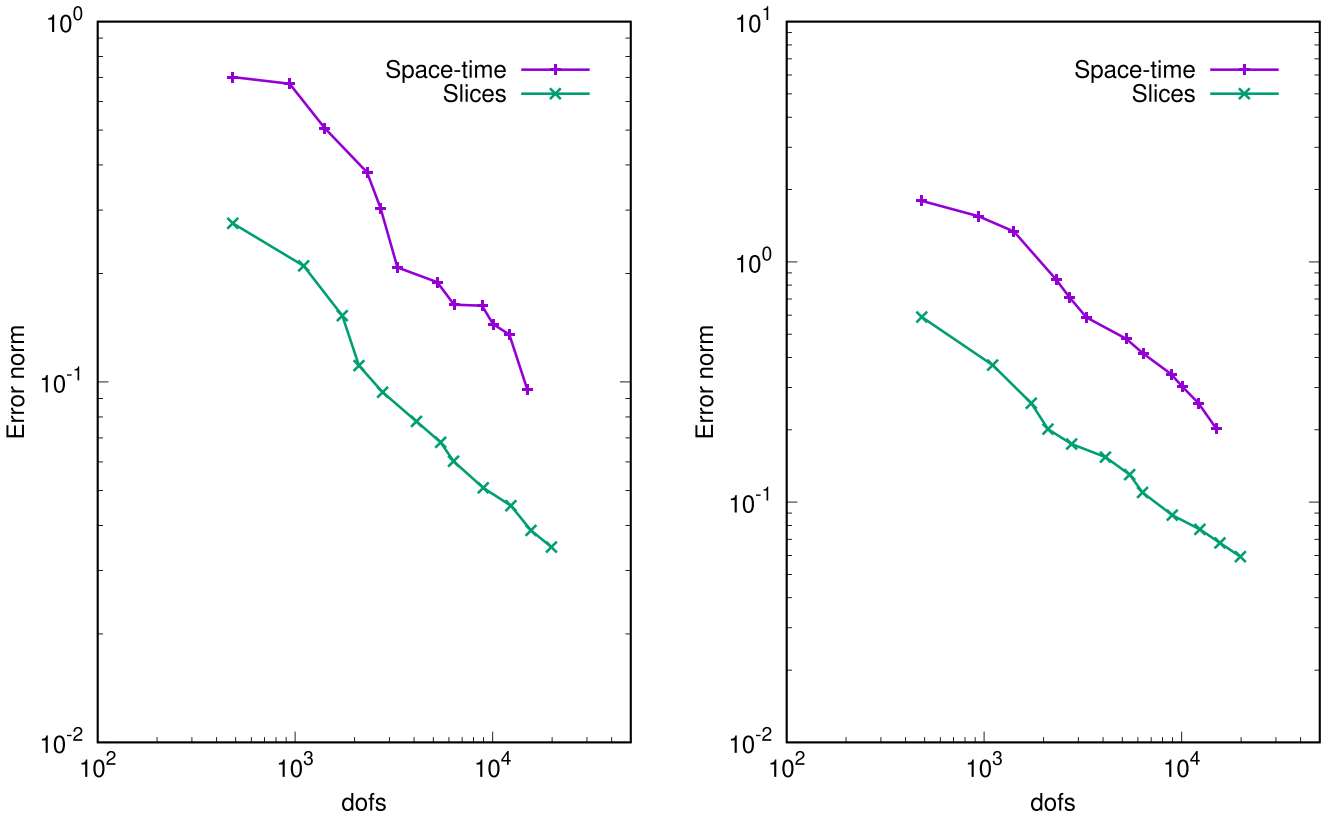

(a) $\|\boldsymbol{\sigma} - \boldsymbol{\sigma}^h\|_{L^2(\Omega_{\mathrm{T}})}$. (b) $\|(\zeta - \zeta^h, \mathbf{u} - \mathbf{u}^h, \boldsymbol{\sigma} - \boldsymbol{\sigma}^h)\|_{\mathrm{B}}$.

Fig. 6 Error convergence results comparing the space-time and time slice approaches

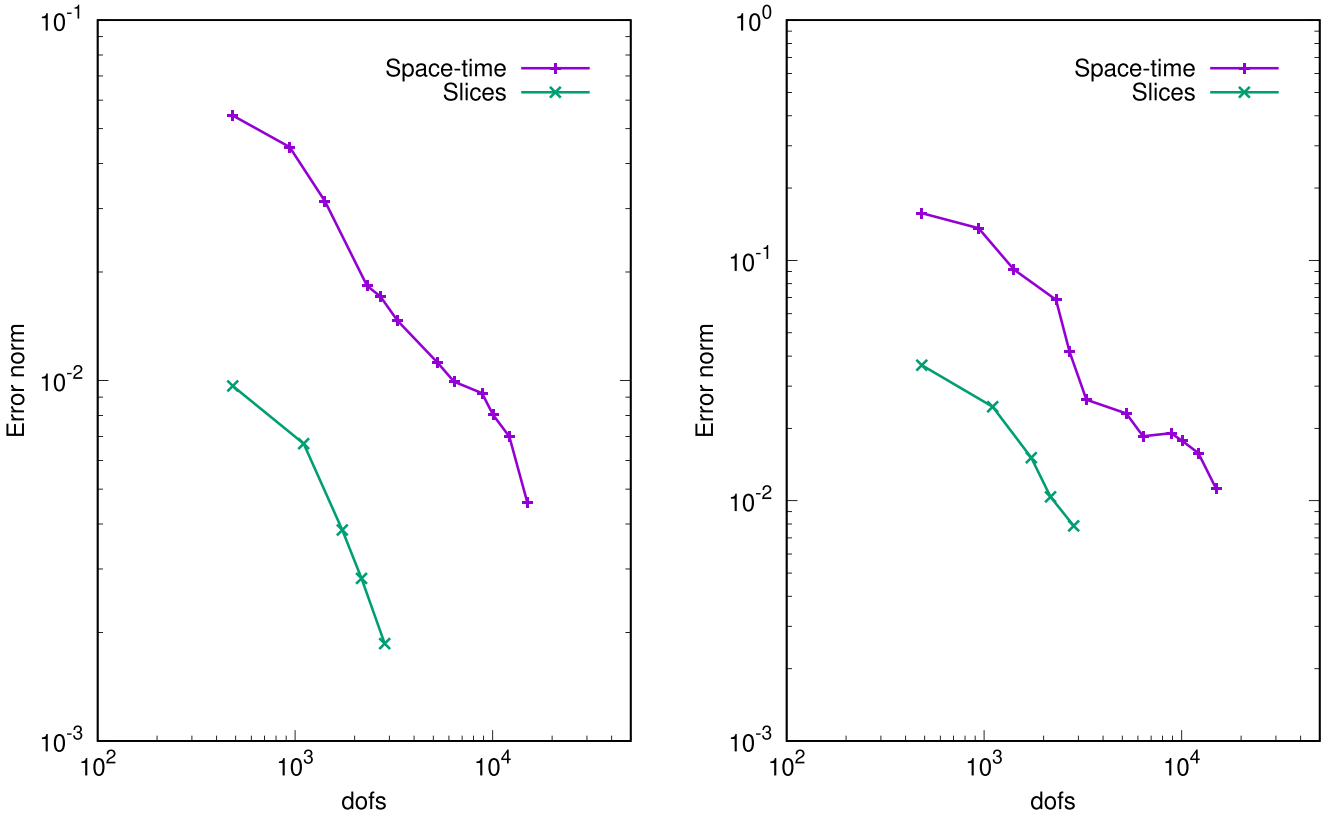

(a) $\|\zeta - \zeta^h\|_{L^2(\Omega_T)}$. (b) $\|\mathbf{u} - \mathbf{u}^h\|_{L^2(\Omega_T)}$.

Fig. 7 Error convergence results comparing the space-time and time slice approaches

presented results. However, the time step used in [15] is $0.25s$ in Euler's method, i.e., the total number of time steps over seven days is roughly 2.4 million, whereas the AVS-FE solution is obtained in a single solution step.

4.6 Dam break

As a final numerical verification, we consider another commonly applied benchmark problem found in literature [29], known as a dam break problem. We consider a one-dimensional case, in which a $2000m$ channel is divided by a dam separating two distinct water levels, i.e., $\Omega = (x_L, x_R) = (0, 2000m)$. In Fig. 10 the set up for the problem is shown. At $t = 0s$, the dam is removed to simulate its total failure allowing the water to flow unconstrained into the lower reservoir. The parameters are $\nu = 10^{-2}m$, $\tau_b = 1s^{-1}$, and we consider a constant bathymetry $h_b(\mathbf{x}) = 0$, and the initial and boundary conditions are:

$$\begin{aligned} &\zeta_0 = 10m, \quad x \leq 1000m \\ &\zeta_0 = 5m, \quad x > 1000m \\ &u_0 = 0, \\ &u(0,t) = 0, \\ &\zeta(2000m,t) = 0. \end{aligned} \tag{36}$$

Hence, we expect sharp interfaces in the resulting velocity and elevation fields, i.e., shocks, to develop. We consider the final time to be $T = 200s$, i.e., the space-time domain is $\Omega_T = (0, 2000m) \times (0, 200s)$. The corresponding AVS-FE discretization employs a uniform mesh of $2(800 \times 35)$

Table 2 Elevation and velocity errors for the lake at rest

$\|\zeta - \zeta^h\|_{L^2(\Omega_T)}$	$\|\mathbf{u} - \mathbf{u}^h\|_{L^2(\Omega_T)}$
$9.02 \cdot 10^{-15}$	$4.00 \cdot 10^{-13}$

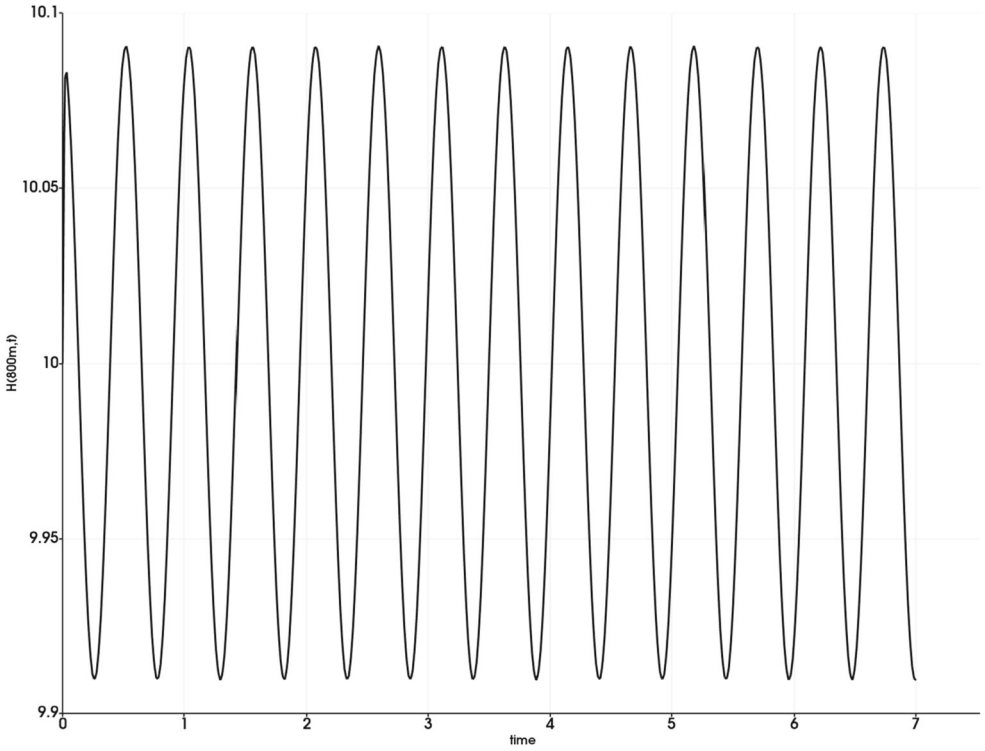

Fig. 8 $H^h(800m, t)$ (m)

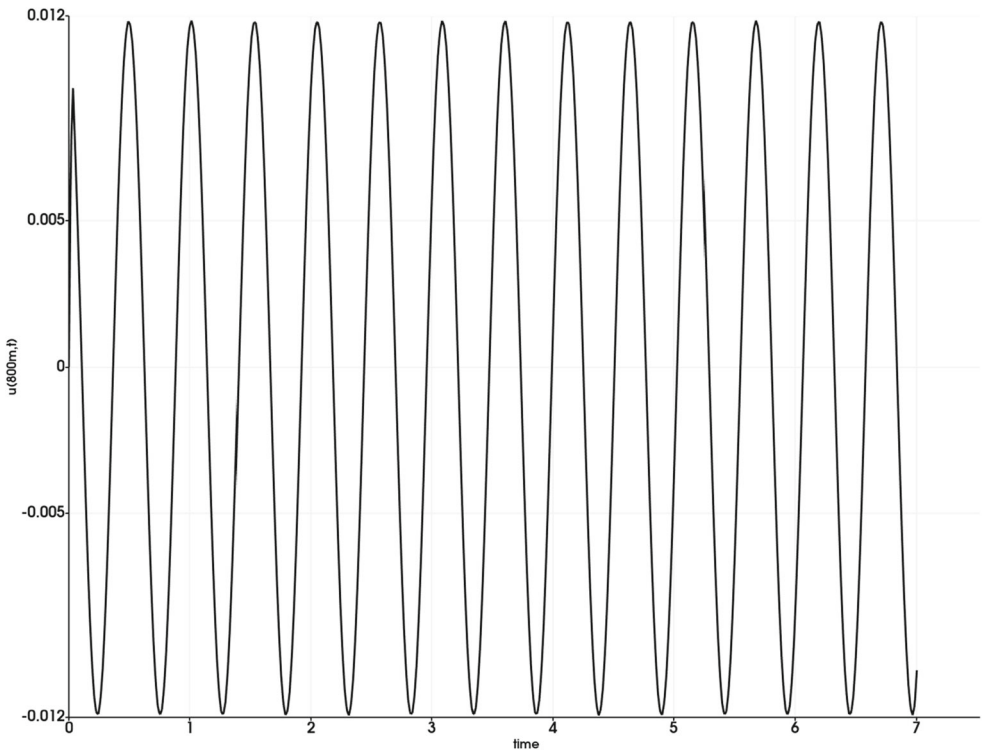

Fig. 9 $u^h(800m, t)$ $(\frac{m}{s})$

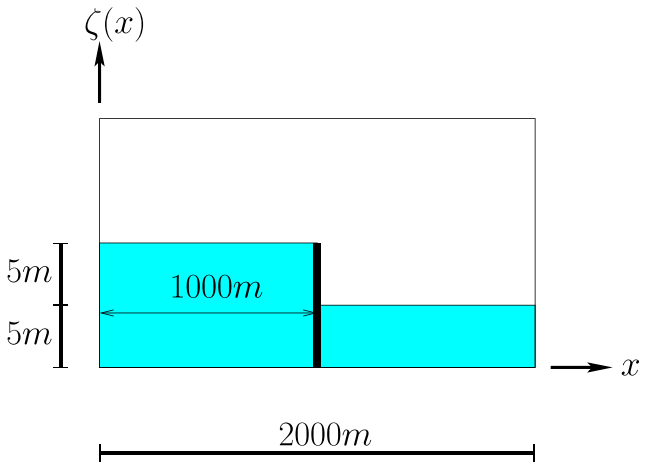

Fig. 10 Dam break problem spatial domain

triangular elements with discrete function spaces as defined in (31) with $p = 2$.

In Fig. 11, we present the elevation profile for select times. As time progresses, the elevation profile stretches out as expected from the boundary and initial conditions. Shortly after the simulated dam break, at $t = 0.1$ seconds, the elevation profile does not exhibit any noticeable oscillations leading to an accurate representation of the shock. Comparison with the results in [29], which uses slightly different boundary and initial conditions, shows good agreement based on visual inspection.

5 Conclusions

We have introduced a stable space-time FE method for the SWE, the AVS-FE method. This Petrov-Galerkin method derives its stability from the DPG concept of optimal test functions. We establish continuous and stable FE approximations in both space and time by introducing a Riesz representation problem governing the optimal test functions. Compared to existing FE technologies for the SWE we do not need to consider surrogate models such as the diffusive wave model or perform arduous problem-dependent analysis to establish proper stabilization parameters to achieve discrete stability.

Consideration of a linearized SWE allows us to establish well posedness of the AVS-FE weak formulation by employing DPG and FOSLS philosophies. Furthermore, for the linearized problem, we establish *a priori* error estimates. The convergence behavior predicted by these estimates is confirmed through a sequence of numerical convergence studies for the full nonlinear SWE. In the case of asymptotic $h-$convergence, we observe optimal rates for all applicable norms of the numerical approximation errors. The built-in error estimate and corresponding error indicators of the AVS-FE approximation error in terms of the energy norm allow us to pursue space-time adaptive mesh refinement strategies.

In an effort to keep the computational cost of the space-time AVS-FE approximations or increase their accuracy,

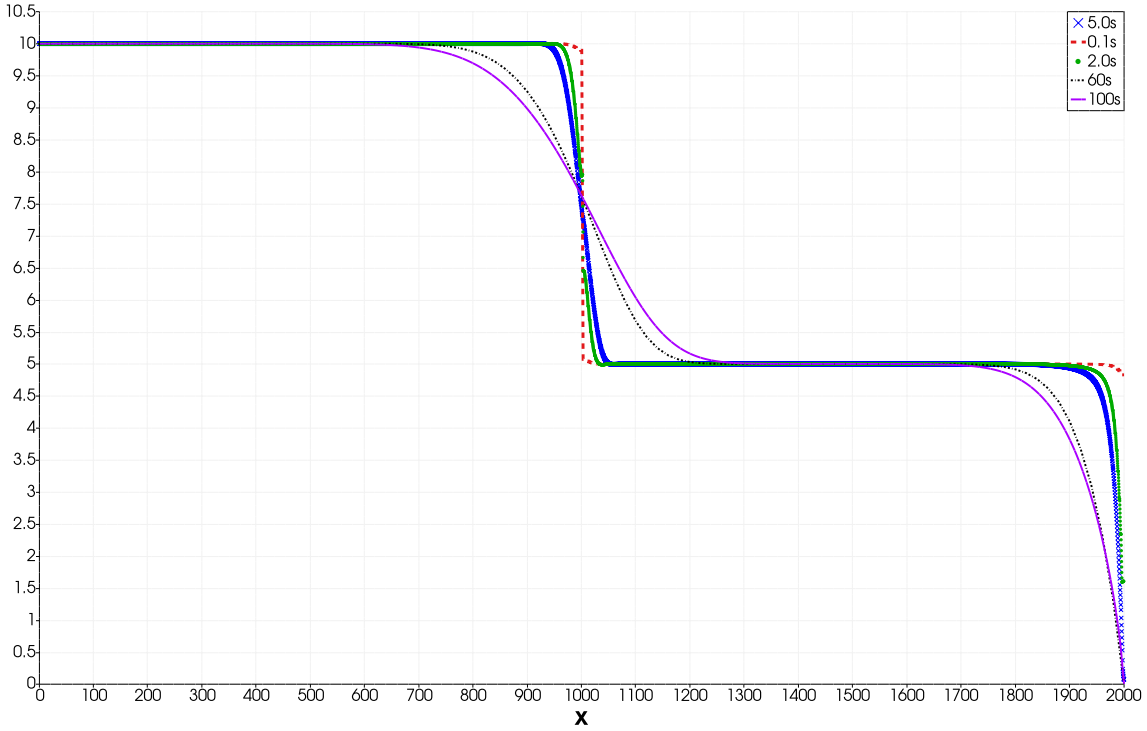

Fig. 11 $\zeta^h(x,t)$ at various times

we also consider a technique in which we partition the space-time domain into space-time slices. This time slice approach allows further localization of the space-time mesh refinements, which now occur on each individual slice. We present numerical verifications in which we consider and compare the space-time and space-time slice approaches to each other. These verifications show that the time slice approach becomes preferable for longer simulations in terms of better accuracy measured in norms of the approximation error. Note that what constitutes a long simulation is problem dependent. For the SWE and the verifications we consider here our experience indicates that the threshold is around one second. We also show that this approach can be used to weigh accuracy versus computational efficiency.

We have considered space-time adaptive mesh refinements using a built-in error estimate of the AVS-FE. However, we are not limited to this type of error estimator, and any *a posteriori* error estimation technique can be applied. In particular, we envision the use of Goal-Oriented error estimates, and their error indicators in terms of local quantities of interest. For the transient portion of the domain, goal-oriented adaptive algorithms such as those developed by Muñoz-Matute et al. [38] are natural candidates.

The results presented in this paper serves as a proof-of-concept of the space-time AVS-FE method applied to the SWE. In particular, we have presented numerical verifications of two important physical processes governed by the SWE, tidal fluctuations and that of a dam failure. In addition to these physical examples, we have also verified the well balanced property of the AVS-FE method applied to the SWE numerically in Section 4.4. Hence, we aim to establish a establish a new paradigm of the application of DPG methods in the mathematical modeling of storm surge events. As these physical processes are complex, occur in complex coastal domains, and exhibit significant temporal variability (e.g., due to changes in wind or rainfall), the local time stepping allowed in the space-time methods is likely to be an important factor to be exploited in future works. Coupling mechanisms such as those established by Choudhary in [14] and by Dawson and Proft in [15] are likely to lead to efficient algorithms in the modeling of storm surge by coupling, e.g., the AVS-FE method and HDG methods [3, 30].

Acknowledgements This work has been supported by the United States National Science Foundation - NSF PREEVENTS Track 2 Program, under NSF Grant Number 1855047.

Data Availability The datasets and computer codes generated in the current study are available from the corresponding author on reasonable request.

References

1. Abhyankar, S., Brown, J., Constantinescu, E.M., Ghosh, D., Smith, B.F., Zhang, H.: Petsc/ts: A modern scalable ode/dae solver library. arXiv:1806.01437 (2018)
2. Alnæs, M.S., Blechta, J., Hake, J., Johansson, A., Kehlet, B., Logg, A., Richardson, C., Ring, J., Rognes, M.E., Wells, G.N.: The FEnics project version 1.5. Arch. Numer. Softw. **3**(100), 9–23 (2015)
3. Arabshahi, H.: Space-time hybridized discontinuous Galerkin methods for shallow water equations. Ph.D. thesis, The University of Texas at Austin, Austin Tx (2016)
4. Babuška, I.: Error-bounds for finite element method. Numer. Math. **16**, 322–333 (1971)
5. Babuška, I., Suri, M.: The *hp* version of the finite element method with quasiuniform meshes. ESAIM: Mathematical Modelling and Numerical Analysis-Modé,lisation Mathématique et Analyse Numérique **21**(2), 199–238 (1987)
6. Balay, S., Abhyankar, S., Adams, M.F., Brown, J., Brune, P., Buschelman, K., Dalcin, L., Dener, A., Eijkhout, V., Gropp, W.D., Karpeyev, D., Kaushik, D., Knepley, M.G., May, D.A., McInnes, L.C., Mills, R.T., Munson, T., Rupp, K., Sanan, P., Smith, B.F., Zampini, S., Zhang, H., Zhang, H.: PETSc users manual. Tech. Rep. ANL-95/11 - Revision 3.12, Argonne National Laboratory. https://www.mcs.anl.gov/petsc (2019)
7. Bochev, P.B., Gunzburger, M.D.: Least-squares finite element methods, vol. 166. Springer Science & Business Media, Berlin (2009)
8. Boffi, D., Brezzi, F., Fortin, M., et al.: Mixed finite element methods and applications, vol. 44 Springer (2013)
9. Brezzi, F., Fortin, M.: Mixed and Hybrid Finite Element Methods, vol. 15 Springer (1991)
10. Calo, V.M., Romkes, A., Valseth, E.: Automatic Variationally Stable Analysis for FE Computations: an Introduction. In: Barrenechea G., Mackenzie, J. (eds.) Boundary and Interior Layers, Computational and Asymptotic Methods BAIL 2018, pp. 19–43. Springer (2020)
11. Carstensen, C., Bringmann, P., Hellwig, F., Wriggers, P.: Nonlinear discontinuous petrov–Galerkin methods. Numer. Math. **139**(3), 529–561 (2018)
12. Carstensen, C., Demkowicz, L., Gopalakrishnan, J.: A posteriori error control for DPG methods. SIAM J. Numer. Anal. **52**(3), 1335–1353 (2014)
13. Carstensen, C., Demkowicz, L., Gopalakrishnan, J.: Breaking spaces and forms for the DPG method and applications including Maxwell equations. Comput. Math. Appl. **72**(3), 494–522 (2016)
14. Choudhary, G.K. et al.: Coupled atmospheric, hydrodynamic, and hydrologic models for simulation of complex phenomena. Ph.D. thesis, The University of Texas at Austin, Austin Tx (2019)
15. Dawson, C., Proft, J.: Discontinuous and coupled continuous/discontinuous Galerkin methods for the shallow water equations. Comput. Methods Appl. Mech. Eng. **191**(41-42), 4721–4746 (2002)
16. Dawson, C., Proft, J.: Discontinuous/continuous Galerkin methods for coupling the primitive and wave continuity equations of shallow water. Comput. Methods Appl. Mechan. Eng. **192**(47-48), 5123–5145 (2003)
17. Demkowicz, L., Gopalakrishnan, J.: A class of discontinuous petrov-Galerkin methods. Part I: The transport equation. Comput. Methods Appl. Mech. Eng. **199**(23), 1558–1572 (2010)
18. Demkowicz, L., Gopalakrishnan, J.: Analysis of the DPG method for the Poisson equation. SIAM J. Numer. Anal. **49**(5), 1788–1809 (2011)
19. Demkowicz, L., Gopalakrishnan, J.: A class of discontinuous petrov-Galerkin methods. II. Optimal test functions. Numer. Methods Partial Differ. Equ. **27**(1), 70–105 (2011)

20. Demkowicz, L., Gopalakrishnan, J.: A class of discontinuous petrov-Galerkin methods. Part III: Adaptivity. Appl. Numer. Math. **62**(4), 396–427 (2012)
21. Demkowicz, L., Zanotti, P.: Construction of DPG Fortin operators revisited. Computers & Mathematics with Applications (2020)
22. Demkowicz, L.F., Gopalakrishnan, J.: An Overview of the Discontinuous Petrov Galerkin Method. In: Recent Developments in Discontinuous Galerkin Finite Element Methods for Partial Differential Equations, pp. 149–180. Springer (2014)
23. Dörfler, W.: A convergent adaptive algorithm for Poisson's equation. SIAM J. Numer. Anal. **33**(3), 1106–1124 (1996)
24. Ellis, T.E.: Space-time discontinuous petrov-Galerkin finite elements for transient fluid mechanics. Ph.D. thesis, The University of Texas at Austin, Austin Tx (2016)
25. Ellis, T.E., Demkowicz, L., Chan, J., Moser, R.D.: Space-time DPG: Designing a method for massively parallel CFD, ICES report. The Institute for Computational Engineering and Sciences. The University of Texas at Austin 14–32 (2014)
26. Falconer, R.: An introduction to nearly horizontal flows. Coastal, estuarial and harbour engineers' reference book 27–36 (1993)
27. Gassner, G.J., Winters, A.R., Kopriva, D.A.: A well balanced and entropy conservative discontinuous Galerkin spectral element method for the shallow water equations. Appl. Math. Comput. **272**, 291–308 (2016)
28. Gopalakrishnan, J., Qiu, W.: An analysis of the practical DPG method. Math. Comput. **83**(286), 537–552 (2014)
29. Jacobs, C.T., Piggott, M.D.: Firedrake-fluids v0. 1: numerical modelling of shallow water flows using an automated solution framework. Geoscientific Model Development **8**(3), 533–547 (2015)
30. Jones, G.S., Lee, J.J., Rhebergen, S.: A space-time hybridizable discontinuous Galerkin method for linear free-surface waves. J. Sci. Comput. **85**(3), 1–38 (2020)
31. Kawahara, M., Hirano, H., Tsubota, K., Inagaki, K.: Selective lumping finite element method for shallow water flow. Int. J. Numer. Methods Fluids **2**(1), 89–112 (1982)
32. Kubatko, E.J., Bunya, S., Dawson, C., Westerink, J.J.: Dynamic p-adaptive runge–Kutta discontinuous Galerkin methods for the shallow water equations. Comput. Methods Appl. Mech. Eng. **198**(21-26), 1766–1774 (2009)
33. LeVeque, R.J.: Balancing source terms and flux gradients in high-resolution godunov methods: the quasi-steady wave-propagation algorithm. J. Comput. Phys. **146**(1), 346–365 (1998)
34. Liang, S.J., Hsu, T.W.: Least-squares finite-element method for shallow-water equations with source terms. Acta Mech. Sinica **25**(5), 597–610 (2009)
35. Luettich, R.A., Westerink, J.J., Scheffner, N.W., et al.: Adcirc: an advanced three-dimensional circulation model for shelves, coasts, and estuaries. Report 1, theory and methodology of ADCIRC-2DD1 and ADCIRC-3DL Computers & fluids (1992)
36. Lynch, D.R., Gray, W.G.: A wave equation model for finite element tidal computations. Computers & fluids **7**(3), 207–228 (1979)
37. Michel-Dansac, V., Berthon, C., Clain, S., Foucher, F.: A well-balanced scheme for the shallow-water equations with topography or manning friction. J. Comput. Phys. **335**, 115–154 (2017)
38. Muñoz-Matute, J., Calo, V.M., Pardo, D., Alberdi, E., van der Zee, K.G.: Explicit-in-time goal-oriented adaptivity. Comput. Methods Appl. Mech. Eng. **347**, 176–200 (2019)
39. Nagaraj, S., Petrides, S., Demkowicz, L.F.: Construction of DPG Fortin operators for second order problems. Comput. Math. Appl. **74**(8), 1964–1980 (2017)
40. Oden, J.T., Reddy, J.N.: An introduction to the mathematical theory of finite elements. Dover Publications (2012)
41. Peraire, J., Zienkiewicz, O., Morgan, K.: Shallow water problems: a general explicit formulation. Int. J. Numer. Methods Eng. **22**(3), 547–574 (1986)
42. Praagman, N.: Numerical solution of the shallow water equations by a finite element method. Ph.D. thesis, Technische Hogeschool Delft, Delft NL (1979)
43. Ribeiro, F., Castro, R., Galeão, A., Loula, A., Landau, L.: A Space-Time Finite Element Formulation for Shallow Water Equations with Shock-Capturing Operator. In: IV World Congress, Argentina (1998)
44. Ribeiro, F., Galeão, A., Castro, R., Landau, L.: Finite elements for shallow water equations: stabilized formulations and computational aspects. WIT Trans. Eng. Sci. 29 (1970)
45. Rivière, B., Wheeler, M.F., Girault, V.: Improved energy estimates for interior penalty, constrained and discontinuous Galerkin methods for elliptic problems. part i. Comput. Geosci. **3**(3-4), 337–360 (1999)
46. Roberts, N.V., Demkowicz, L., Moser, R.: A discontinuous petrov–Galerkin methodology for adaptive solutions to the incompressible navier–Stokes equations. J. Comput. Phys. **301**, 456–483 (2015)
47. Salazar, J., Mora, J., Demkowicz, L.: Alternative enriched test spaces in the DPG method for singular perturbation problems. Comput. Methods Appl. Math. **19**(3), 603–630 (2019)
48. Samii, A., Kazhyken, K., Michoski, C., Dawson, C.: A comparison of the explicit and implicit hybridizable discontinuous Galerkin methods for nonlinear shallow water equations. J. Sci. Comput. **80**(3), 1936–1956 (2019)
49. Starke, G.: A first-order system least squares finite element method for the shallow water equations. SIAM J. Numer. Anal. **42**(6), 2387–2407 (2005)
50. Storn, J.: On a relation of discontinuous Petrov–Galerkin and least-squares finite element methods. Comput. Math. Appl. **79**(12), 3588–3611 (2020)
51. Takase, S., Kashiyama, K., Tanaka, S., Tezduyar, T.E.: Space–time SUPG formulation of the shallow-water equations. Int. J. Numer. Methods Fluids **64**(10-12), 1379–1394 (2010)
52. Valseth, E., Dawson, C.: An unconditionally stable space–time FE method for the Korteweg–de Vries equation. Comput. Methods Appl. Mech. Eng. **371**, 113297 (2020)
53. Wintermeyer, N., Winters, A.R., Gassner, G.J., Kopriva, D.A.: An entropy stable nodal discontinuous Galerkin method for the two dimensional shallow water equations on unstructured curvilinear meshes with discontinuous bathymetry. J. Comput. Phys. **340**, 200–242 (2017)
54. Wu, X., Kubatko, E.J., Chan, J.: High-order entropy stable discontinuous Galerkin methods for the shallow water equations: curved triangular meshes and GPU acceleration. Comput. Math. Appl. **82**, 179–199 (2021)